X-ray Population Study in the Small Magellanic Cloud with ASCA

Jun Yokogawa

Department of Physics, Graduate School of Science,
Kyoto University, Sakyo-ku, Kyoto 606-8502, Japan

Submitted to the Department of Physics,
Kyoto University on February 1, 1999,
in partial fulfillment of the requirements
for the degree of Master of Science.

This thesis will be available at
http://www-cr.scphys.kyoto-u.ac.jp/member/jun/job/.

Abstract

The Advanced Satellite for Cosmology and Astrophysics (ASCA) has made multiple pointing observations on the Small Magellanic Cloud (SMC). The X-ray mosaic images in the soft (0.7–2.0 keV) and hard (2.0–7.0 keV) band are separately constructed, and the later provides the first hard X-ray image of the SMC. We extracted 39 sources from these images with a criterion of $S/N > 5$. Spectral and timing analyses were performed for all of these sources. Coherent pulsations were detected from 12 X-ray sources; five are newly discovered X-ray pulsars. Most of the 12 X-ray pulsars are found to exhibit long-term variabilities. Hence they are likely to be X-ray binary pulsars (XBPs). We find that XBPs and thermal supernova remnants in the SMC are clearly separated by the hardness ratio (ratio of the count rate between hard and soft band). Presence of more XBPs in the SMC is suggested from this empirical grouping. Possible implications on the star-formation history and galaxy evolution of the SMC are presented based on comparison between the X-ray population in the SMC and that in our Galaxy.

Contents

1 Introduction **1**

2 Review on the Small Magellanic Cloud **3**

2.1 Overview 4

2.1.1 The Magellanic System 4

2.1.2 Interaction between the Magellanic Clouds and our Galaxy 5

2.1.3 Features of the SMC 6

2.2 High energy aspects 8

2.2.1 Previous X-ray observations 8

2.2.2 Previous γ-ray observations 10

3 Instruments **12**

3.1 Overview of the ASCA satellite 12

3.2 XRT: X-ray Telescope 12

3.3 GIS: Gas Imaging Spectrometer 15

3.4 SIS: Solidstate Imaging Spectrometer 18

4 Observations and Data Reduction **24**

5 Results **25**

5.1 X-ray images 25

5.1.1 Images and source extraction 25

5.1.2 Definition of the hardness ratio 27

5.2 Timing analyses 27

5.3 Spectral analyses 32

5.3.1 X-ray pulsars and HMXBs 32

5.3.2 SNRs 33

5.3.3 The other sources . . . 38
5.4 X-ray pulsars . . . 40
5.4.1 No. 38: SMC X-1 . . . 40
5.4.2 No. 25: RX J0059.2−7138 . . . 43
5.4.3 2E0050.1−7247 . . . 43
5.4.4 No. 11: AX J0051−722 . . . 45
5.4.5 No. 15: 1WGA J0053.8−7226 . . . 46
5.4.6 XTE J0054−720 . . . 47
5.4.7 No. 16: XTE J0055−724 . . . 47
5.4.8 No. 3: AX J0049−729 . . . 47
5.4.9 No. 8: AX J0051−733 . . . 49
5.4.10 No. 20: AX J0058−720 . . . 50
5.4.11 No. 29: 1SAX J0103.2−7209 . . . 51
5.4.12 No. 32: AX J0105−722 . . . 53
5.4.13 No. 5: AX J0049−732 . . . 55
5.4.14 No. 37: XTE J0111.2−7317 . . . 55
5.4.15 No. 14: RX J0052.1−7319 . . . 55
5.5 The 1st ASCA catalogue of X-ray sources in the SMC . . . 57

6 Discussion **60**
6.1 Classification with hardness ratio . . . 60
6.1.1 XBPs and thermal SNRs in the SMC . . . 60
6.1.2 Including the LMC samples . . . 60
6.1.3 Validity of our classification method . . . 64
6.1.4 Candidates of XBPs and thermal SNRs . . . 65
6.2 Population in the SMC . . . 67

7 Conclusion **70**

List of Figures

2.1 Optical images of the Magellanic Clouds 3
2.2 HI distribution in the Magellanic System 4
2.3 Distances to Cepheids in the SMC 6
2.4 X-ray view of the SMC in late 1970's 8
2.5 X-ray view of the SMC obtained with Einstein 9
2.6 X-ray view of the SMC obtained with ROSAT 10

3.1 Schematic view of ASCA 13
3.2 Mechanism of an X-ray telescope 13
3.3 Effective area of XRT vs. X-ray energy 14
3.4 Effective area of XRT vs. off-axis angle 14
3.5 Point spread function of XRT 15
3.6 Stray light of XRT 16
3.7 Schematic view of GIS 17
3.8 Effective area of GIS with XRT 18
3.9 SIS chip configuration 20
3.10 Effective area of SIS with XRT 20
3.11 Grade definition for an SIS event 22

5.1 SMC mosaic contour images 26
5.2 HR vs. raw count rate 28
5.3 Searching for coherent pulsations from AX J0105−722 29
5.4 History of discoveries of X-ray pulsars in the SMC 30
5.5 SIS spectra of 0103−726 35
5.6 Confidence contours between kT and τ (0103−726) 36
5.7 SIS spectra of N19 and N66 37
5.8 GIS spectra of 0049−736, 0056−725 and DEM S128 39

5.9 Pulse period history of SMC X-1 41
5.10 Spectra and folded light curves of SMC X-1 42
5.11 Spectrum and folded light curves of RX J0059.2−7138 44
5.12 Spectrum and folded light curves of AX J0051−722 45
5.13 Spectrum and folded light curves of 1WGA J0053.8−7226 46
5.14 Spectrum and folded light curves of XTE J0055−724 48
5.15 Spectrum and folded light curves of AX J0049−729 49
5.16 Spectrum and folded light curves of AX J0051−733 50
5.17 Spectrum and folded light curves of AX J0058−720 51
5.18 Spectrum and folded light curves of 1SAX J0103.2−7209 52
5.19 Spectrum and folded light curves of AX J0105−722 54
5.20 Spectrum and folded light curves of XTE J0111.2−7317 56

6.1 HR vs. raw count rate for the classified sources (SMC) 61
6.2 HR vs. flux for the classified sources (SMC) 62
6.3 HR vs. observed luminosity for the classified sources (SMC & LMC) 64
6.4 HR vs. observed luminosity for all sources (SMC) and the classified sources (LMC) 66

List of Tables

3.1 Basic properties of GIS 16
3.2 Bit assignment for GIS 19
3.3 Temporal properties of GIS 19
3.4 Basic properties of SIS 19
3.5 Temporal properties of SIS 21

4.1 Observed fields 24

5.1 X-ray pulsars in the SMC 31
5.2 Line intensities in the SNR spectra 34
5.3 Spectral parameters of 0103−726 35
5.4 Spectral parameters of N19 and N66 37
5.5 Spectral parameters of 0049−736, 0056−725 and DEM S128 39
5.6 Spectral parameters of SMC X-1 41
5.7 Spectral parameters of RX J0059.2−7138 44
5.8 Spectral parameters of AX J0051−722 45
5.9 Spectral parameters of 1WGA J0053.8−7226 46
5.10 Changes of flux and pulse period of XTE J0055−724 48
5.11 Spectral parameters of XTE J0055−724 48
5.12 Spectral parameters of AX J0049−729 49
5.13 Spectral parameters of AX J0051−733 50
5.14 Spectral parameters of AX J0058−720 51
5.15 Spectral parameters of 1SAX J0103.2−7209 52
5.16 Spectral parameters of AX J0105−722 54
5.17 Spectral parameters of XTE J0111.2−7317 56
5.18 The 1st ASCA catalogue of X-ray sources in the SMC 58

6.1 HRs under different absorption column densities 65

6.2 Non-pulsating HMXBs in the SMC 67
6.3 Populations in the SMC and our Galaxy 68

Chapter 1

Introduction

Studies of X-ray population in a whole galaxy provide direct information on the history of evolution, such as formation of stars and binaries. A Crab-like supernova remnant (SNR) is a descendant of a high-mass star, while a binary system of high-mass stars evolves into a high-mass X-ray binary (HMXB). Hence existence of them indicates a star-formation activity about 10^6–10^7 yr ago. On the other hand, low-mass X-ray binaries (LMXBs) are generally considered to be formed when a neutron star is captured by a low-mass star. Therefore existence of LMXBs is evidence of star-formation about 10^8 yr ago or more.

X-ray surveys of a whole galaxy are necessary for population studies. The Small Magellanic Cloud (SMC) is the best target, because of its small angular sizes ($\sim 3^\circ \times 3^\circ$), proximity (60 kpc is assumed in this paper) and low interstellar absorption toward it. Such surveys have been carried out with previous X-ray satellites Einstein and ROSAT. Most complete source catalogues are presented in Wang & Wu (1992, hereafter WW92) and Kahabka et al. (1999, hereafter K99). Finding of optical counterparts of ROSAT sources were systematically performed in Cowley et al. (1997) and Schmidtke et al. (1998). They revealed five HMXBs.

However, source classification is generally a difficult problem. K99 classified the ROSAT sources according to two kinds of spectral hardness ratios and source extent, still leaving some misidentification.

In this paper, we aim to establish a simple and reliable classification method in the SMC with ASCA. A brief review on the SMC is given in chapter 2. The ASCA satellite and its equipment are described in chapter 3. Observation fields and the method of data reduction are presented in chapter 4. In chapter 5, sources are extracted from X-ray images, then timing and spectral analyses are performed on all the sources. Some of the detected SNRs are categorized as thermal SNRs, while most of the detected X-ray pulsars are regarded as X-ray binary pulsars

(XBPs). In chapter 6, we show that only one hardness ratio is necessary to distinguish between thermal SNRs and XBPs. After discussing the validity of this method, candidates of the two classes are defined. Then population in the SMC is discussed. Finally, we summarize this study in chapter 7.

Chapter 2

Review on the Small Magellanic Cloud

Nights in the southern hemisphere are, different from those in the northern hemisphere, decorated with the two diffuse clouds besides the Milky Way: the Large Magellanic Cloud (LMC) and the Small Magellanic Cloud (SMC). We present a review on them, particularly on the SMC.

Figure 2.1: Optical images of the LMC (left) and the SMC (right). Optical Wing is protruding out from the main body of the SMC to the east (left side in the figure). (©Anglo-Australian Observatory)

2.1 Overview

2.1.1 The Magellanic System

The SMC and LMC (Magellanic Clouds) are the satellite galaxies orbiting around our Galaxy. Both of them have an optically bar-like structure (figure 2.1). The dimensions and locations (equatorial coordinates in J2000) of the bars are $\sim 2.5^\circ \times 1^\circ$ and $(0^h53^m, -72^\circ50')$ for the SMC, and $\sim 3^\circ \times 1^\circ$ and $(5^h23^m, -69^\circ44')$ for the LMC, respectively. An optical "Wing" is protruding out from the main body of the SMC to the east, i.e. in the direction of the LMC. The Magellanic Clouds have a common HI envelope and an HI feature extending between them ("Bridge"). In addition, between the Magellanic Clouds and our Galaxy, there exist two streams of HI gas. One is "the Magellanic Stream" discovered by Mathewson, Cleary & Murray (1974) and the other is "the Leading Arm" discovered very recently by Putman et al. (1998). These structures are, as a whole, called the Magellanic System (figure 2.2).

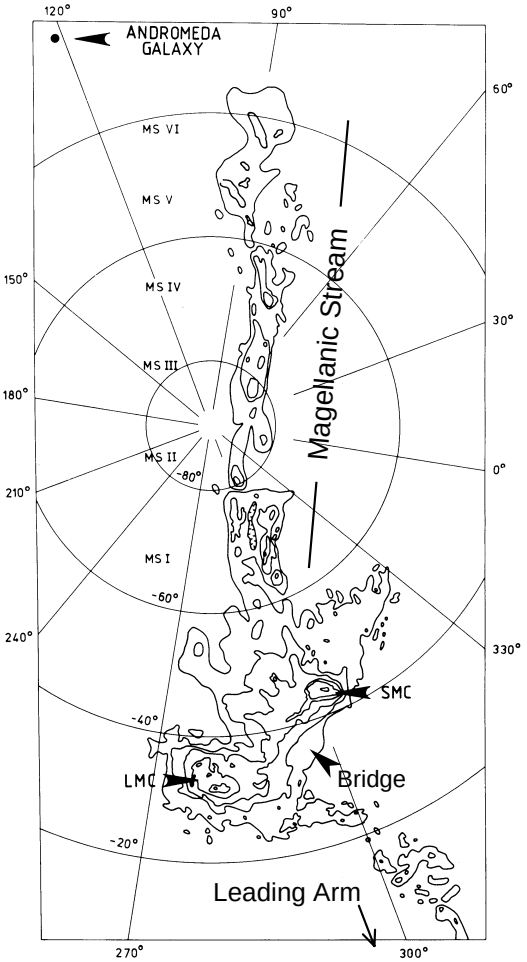

Figure 2.2: Global distribution of HI in the Magellanic System, taken from Mathewson (1985). Coordinates are in Galactic. The Leading Arm was discovered later on (Putman et al. 1998).

2.1.2 Interaction between the Magellanic Clouds and our Galaxy

There are several pieces of evidence which indicate interactions between the Magellanic Clouds and our Galaxy. The existence of the optical Wing of the SMC, sticking out in the direction to the LMC, and the HI Bridge is indicative of interactions between the two Clouds. Stars in the Bridge and around the tip of the SMC Wing were found to be as young as 10^8 yr, suggesting their common origin (Irwin, Demers & Kunkel 1990). Vallenari et al. (1996) investigated the ages of stars outside the main body of the LMC and concluded that stars in the western side (direction to the Bridge) are youngest (2–3 $\times 10^9$ yr) among their survey fields. The existence of young stars (10^{8-9} yr) in and around the Bridge is a hint of tidal interactions which influenced the star-forming activity (Vallenari et al. 1996). The Leading Arm and the Magellanic Stream indicate interactions between the Clouds and our Galaxy. The former is leading the motion of the Clouds while the latter is a trailing stream. The idea that both the streams were torn from the Clouds by tidal interactions is favored because the existence of both the leading and trailing stream is naturally expected in tidal interactions (Putman et al. 1998).

Many numerical simulations of orbits of the Clouds and our Galaxy have been performed to reproduce the Bridge and the Magellanic Stream via such tidal interactions (e.g. Murai & Fujimoto 1980; Gardiner, Sawa & Fujimoto 1994; Gardiner & Noguchi 1996). Murai & Fujimoto (1980) showed that the Magellanic Clouds have been a binary galaxy system for a long time ($\sim$ 10 Gyr), which is consistent with the existence of the common HI envelope. They also showed that the Magellanic Stream was torn off from the SMC by tidal force and that the two Clouds experienced a close encounter about 2×10^8 yr ago, which synchronizes with the ages of stars in the Bridge. Recently, two observational constraints have been obtained. One is the direct measurement of the proper motion of the SMC and LMC with the Hipparcos satellite (Kroupa & Bastian 1997). The proper motion in equatorial longitude and that in equatorial latitude are $(1.23 \pm 0.84,\ -1.21 \pm 0.75)$ mas yr^{-1} for the SMC and $(1.94 \pm 0.29,\ -0.14 \pm 0.36)$ mas yr^{-1} for the LMC. The other is the study of age distribution of star clusters in the LMC by Girardi et al. (1995): the LMC had experienced enhanced cluster formation about 2×10^9 yr and 1×10^8 yr ago. Turbulence of the interstellar matter triggered by two close encounters may have resulted in such bursts of cluster formation. Sawa, Fujimoto & Kumai (1999) showed that some orbits with two close encounters 3×10^9 yr ago and 2×10^8 yr ago could reproduce the Magellanic Stream and were consistent with the Hipparcos measurement. It is open to question whether these orbits can explain other features of the Magellanic System, such as the Leading Arm.

2.1.3 Features of the SMC

The mass of the SMC is about $\sim 2 \times 10^9 M_\odot$, i.e. $\sim 1\%$ of that of our Galaxy. On the other hand, the ratio of HI mass to the total mass is about 30%, which is 30 times larger than the same in our Galaxy. Interstellar medium in the SMC is metal-poor: the abundance of heavy elements is only $\sim 20\%$ of that in the Solar vicinity (Russell & Dopita 1992). These facts indicate that the SMC is a young galaxy, i.e. there still remains sufficient mass from which stars are born. Indeed, there are a lot of young globular-shaped clusters ("populous clusters") in the SMC, which indicates that an active star-formation is still ongoing.

There have been many attempts to determine the distance of the SMC (and LMC). Major methods are the period-luminosity (PL) and period-luminosity-color (PLC) relations of the Cepheids, and the absolute magnitude of RR Lyrae variables. With the aid of these methods, the distance to the SMC is estimated to be about 60 kpc. Some more methods are used to determine the distance to the LMC, and it is derived to be about 50 kpc. We assume above values in this paper.

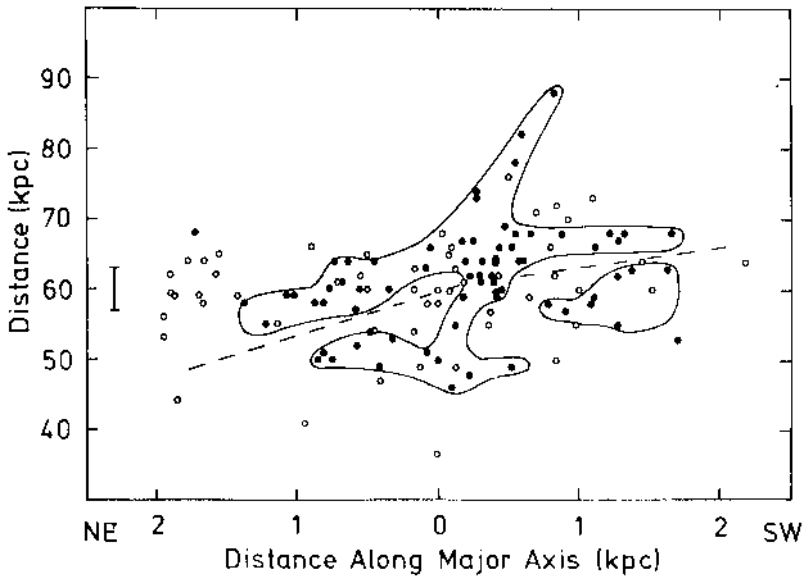

Figure 2.3: Distances to 161 Cepheids in the SMC plotted against their projected distances along the major axis of the SMC (taken from Mathewson, 1985). The filled/open circles represent Cepheids with periods longer/shorter than 10 days (or younger/older than 5×10^7 yr). The solid lines envelope the younger Cepheids. The dashed line demarcates HI component with the low velocity (near) and that with the high velocity (far).

Determination of the distance to each Cepheid can also reveal a three-dementional structure of the galaxy. Mathewson (1985) presented the distances to 161 Cepheids, then the depth of the SMC was revealed to be 20–30 kpc (figure 2.3). It is significantly larger than the projected size of the SMC ($\sim 3^\circ = 4$ kpc), i.e. the SMC has a large inclination angle.

Several studies have been made on the dynamical state of the interstellar matter in the SMC. McGee & Newton (1981) examined the data of HI observations and found that there are four velocity components in the HI profile. Distances and radial velocities of Cepheids were systematically studied by Mathewson, Ford & Visvanathan (1988). They found that certain groups of Cepheids showed the velocity-distance correlation of 4 km s^{-1} kpc^{-1}: more distant Cepheids have larger velocities. They concluded that the SMC is in a process of irreversible disintegration. On the other hand, Caldwell & Coulson (1986) also studied on Cepheids and concluded the SMC is a one-body galaxy with a large velocity gradient in itself. Observations of γ-rays and non-thermal radio emission and calculations of the cosmic ray density described in subsection 2.2.2 prefer the disrupted state of the SMC (Sreekumar & Fichtel 1991).

2.2 High energy aspects

2.2.1 Previous X-ray observations

X-ray observations on the SMC can be traced back to early 1970's. SMC X-1, the first X-ray source in the SMC, was discovered by a rocket flight (Price et al. 1971). Coherent pulsations with 0.716 s period were discovered from SMC X-1 later on (Lucke et al. 1976). Next two sources, SMC X-2 and SMC X-3, were discovered with SAS-3 (Clark et al. 1978). These three sources are considered to be HMXBs today. X-ray view of the SMC at that time is shown in figure 2.4.

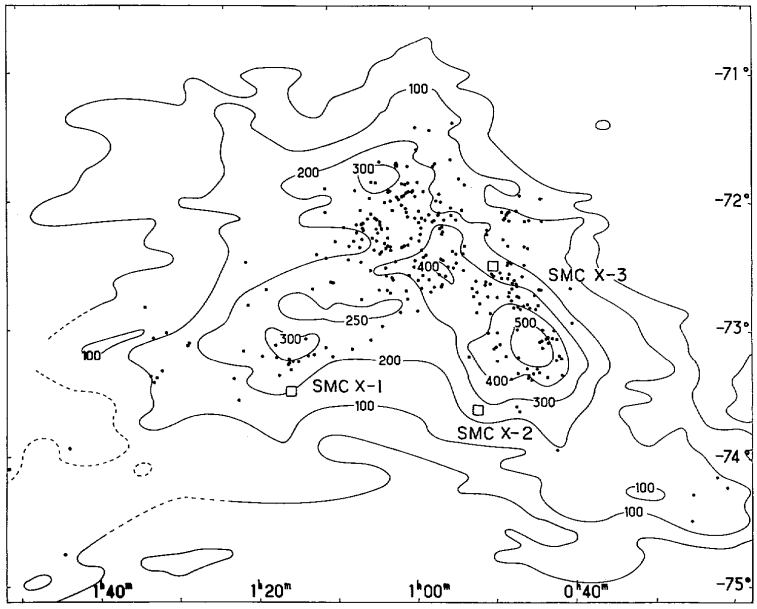

Figure 2.4: X-ray view of the SMC in late 1970's taken from Clark et al. (1978). The position of the three X-ray sources SMC X-1, SMC X-2 and SMC X-3 are shown by squares. The equatorial coordinates (1950B) are presented. Contours and dots represent the surface brightness of 21 cm radio emission and the positions of O–B2 stars, respectively.

The Einstein satellite, which was sensitive to soft X-rays (below a few keV) and had an imaging capability, discovered a large number of X-ray sources. There are 70 catalogued sources (including foreground and background objects) in WW92 (figure 2.5). Some of these sources were identified with radio SNRs, HII regions and known HMXBs while over a half of them were left to be unidentified.

The ROSAT satellite greatly enhanced the number of X-ray sources in the SMC. K99

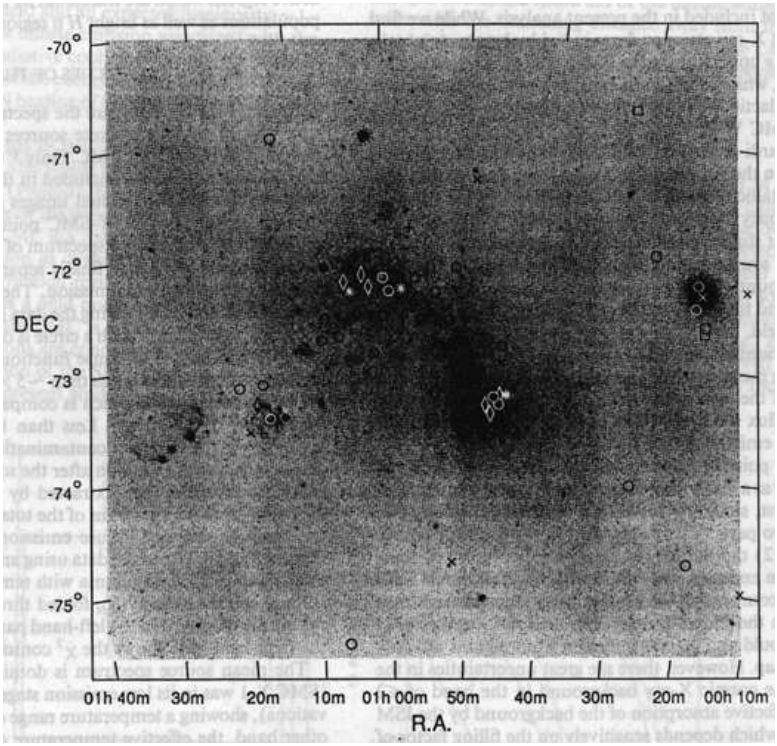

Figure 2.5: X-ray view of the SMC obtained with Einstein superposed on an H_α+[N_{II}] map (taken from WW92). The equatorial coordinates (1950B) are presented. Symbols represent OB associations (asterisks), SNRs (diamonds), unidentified sources (open circles), X-ray binaries (plus signs), foreground Galactic stars (crosses) and background AGNs (open squares).

presented the first ROSAT catalogue of 248 SMC sources (including foreground and background objects; figure 2.6). Cowley et al. (1997) and Schmidtke et al. (1998) determined accurate source positions with ROSAT HRI, then found optical counterparts. Five X-ray sources were identified with Be stars, hence are regarded as HMXBs. A systematic search for X-ray binaries was carried out by Kahabka & Pietsch (1996). They examined flux variability or transient behaviour, and seven sources were accepted as binary candidates. Supersoft X-ray source (SSS) was established as a new source category on the basis of ROSAT observations. Sources of this kind have very soft X-ray spectra with a blackbody temperature of 15–80 eV (Kahabka & van den Heuvel 1997). Kahabka, Pietsch & Hasinger (1994) showed the spectral and temporal properties of five SSSs in the SMC.

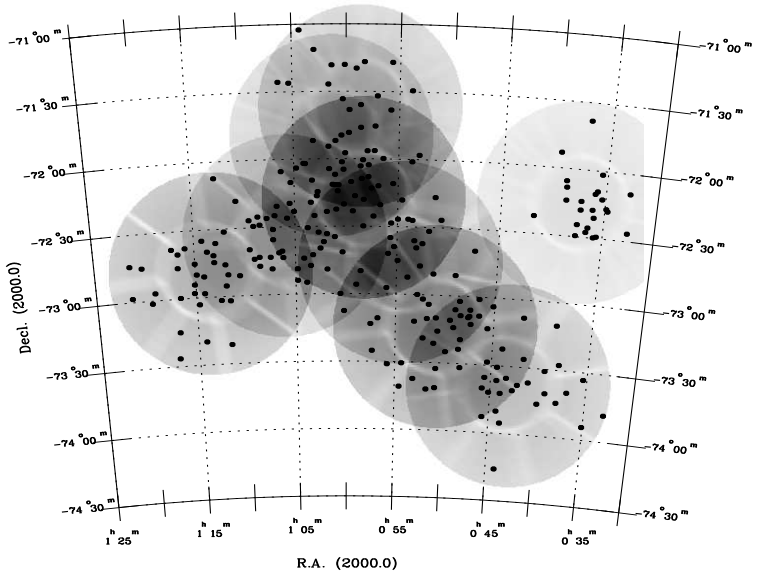

Figure 2.6: X-ray view of the SMC obtained with ROSAT overlaid with the integrated exposure map (taken from K99). The equatorial coordinates (J2000) are presented. Dots represent the detected sources.

2.2.2 Previous γ-ray observations

GeV γ-ray observations were carried out with CGRO EGRET (Sreekumar et al. 1993). The result was negative, giving an upper limit for γ-ray emission at energies > 100 MeV to be 0.5×10^{-7} photon cm^{-2} s^{-1}. GeV γ-rays are produced via the interaction between cosmic ray nucleons and the interstellar matter as follows:

$$\begin{aligned} p + p &\rightarrow p + p + \pi^0 + \cdots, \\ \pi^0 &\rightarrow 2\gamma. \end{aligned}$$

Therefore these γ-rays carry the direct information on the cosmic ray density.

Sreekumar & Fichtel (1991) calculated the γ-ray emission from the SMC based on the HI measurement, non-thermal (synchrotron) radio observations and assumptions of the dynamical state. They derived the cosmic ray density from the radio data, then the γ-ray emission via the interaction between cosmic rays and the HI interstellar matter was calculated. Thus derived flux above 100 MeV was $\sim 10^{-8}$ photon cm^{-2} s^{-1}. It is consistent with the EGRET result (flux $< 0.5 \times 10^{-7}$ photon cm^{-2} s^{-1}). The amount of cosmic rays per unit mass of the interstellar matter was found to be several times smaller than that in our Galaxy. Sreekumar

& Fichtel (1991) concluded that it could be attributed to the dynamical state in the SMC: the interstellar matter in the SMC is not dynamically stable and rather leaky for cosmic rays.

TeV γ-ray observations of the SMC were carried out with a Cerencov telescope (Allen et al. 1993). The intensity of γ-rays in the direction of SMC X-1 showed positive excess, although it was not statistically significant. They gave upper limits of γ-ray flux above 30 TeV from SMC X-1 and the whole SMC as 2.6×10^{-13} photon cm^{-2} s^{-1} and 19.3×10^{-13} photon cm^{-2} s^{-1} msr^{-1}, respectively.

Chapter 3

Instruments

3.1 Overview of the ASCA satellite

ASCA (Advanced Satellite for Cosmology and Astrophysics: Tanaka, Inoue & Holt 1994) is the 4th Japanese satellite for X-ray astronomy launched on Feb. 20, 1993.

ASCA has four X-ray telescopes (XRTs, Serlemitsos et al. 1995) and four instruments at the focal planes: two Gas Imaging Spectrometers (GISs, Ohashi et al. 1996) and two Solidstate Imaging Spectrometers (SISs, Burke et al. 1994). The equipments make it possible to obtain simultaneously X-ray images and spectra in the 0.5–10.0 keV band.

3.2 XRT: X-ray Telescope

X-rays can be totally reflected if their incident angle is smaller than the critical value of the order $\sim 1^{\circ}$. The critical value is smaller for higher energy X-rays. Mirrors of X-ray telescopes which utilize this mechanism are usually placed in Wolter type-I configuration: a combination of a parabolic and hyperbolic shells. Incident X-rays are reflected in series by each of the shells, and focused on the focal plane (see figure 3.2). Effective area can be increased by nesting the shells with a commons focus. Previous X-ray satellites Einstein and ROSAT had this type of X-ray mirrors and provided high resolution images up to a few keV.

However, this type of mirror is heavy, hence a telescope with a large effective area can not be launched with a satellite. Therefore an approximation of the Wolter type-I configuration, which consists of two conical foils, is adopted for XRTs of ASCA. To get a large effective area for higher energy X-rays, the incident angle of each foil should be smaller, which results in a smaller projected area. Nesting a large number of foils compensates for this. According to this

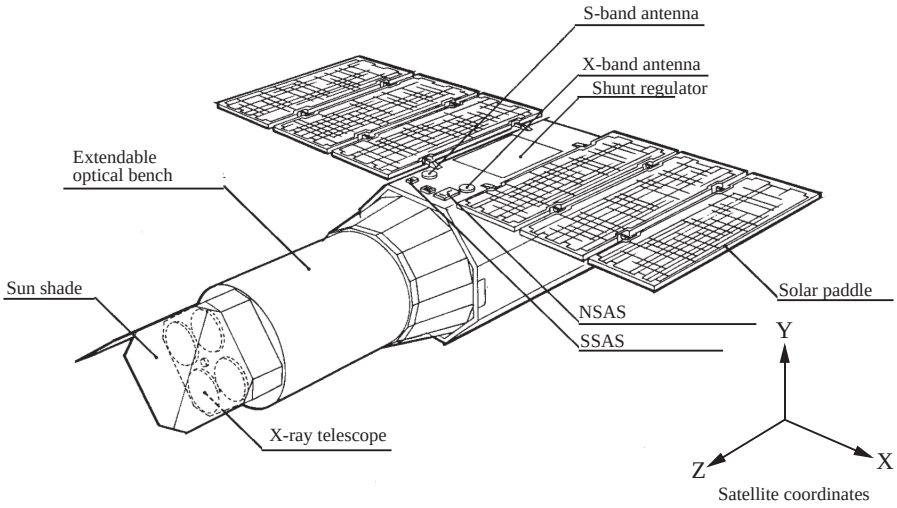

Figure 3.1: Schematic view of ASCA in orbit.

concept, each foil of ASCA XRTs was made to be thin (125 μm) and 120 such foils were nested in a coaxial configuration into one quadrant. As a result, the field of view (FOV) is 18′–24′ (FWHM) and effective area of each XRT is $\sim$ 300 cm^2 below 2 keV and $\sim$ 50 cm^2 at 10 keV. The sum of the effective areas of four XRTs is about 5 or 2 times larger than that of Einstein or ROSAT at $\sim$ 1 keV. Plots of effective area of a single XRT against incident X-ray energy and off-axis angle are shown in figure 3.3 and figure 3.4, respectively.

However, utilizing an approximation of Wolter type-I configuration and very thin foils resulted in a poorer ability of focusing. Figure 3.5 shows the point spread function (PSF) at

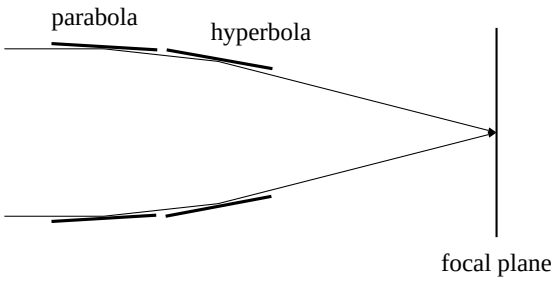

Figure 3.2: Mechanism of an X-ray telescope which utilizes Wolter type-I optics.

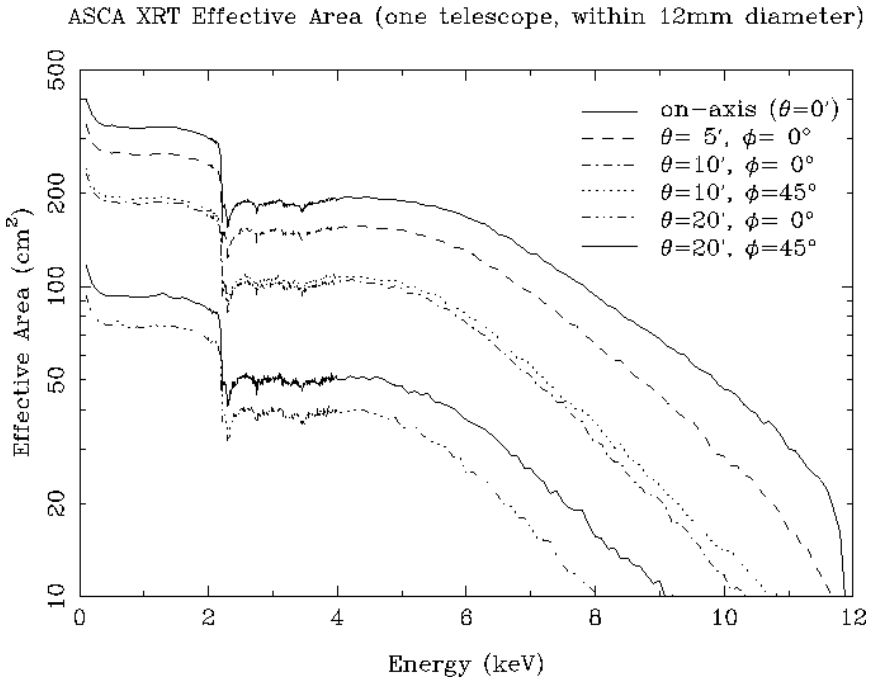

Figure 3.3: Effective area of a single XRT as a function of the energy of the incident X-ray. Dependence on the off-axis angle θ and azimuthal angle ϕ is also shown.

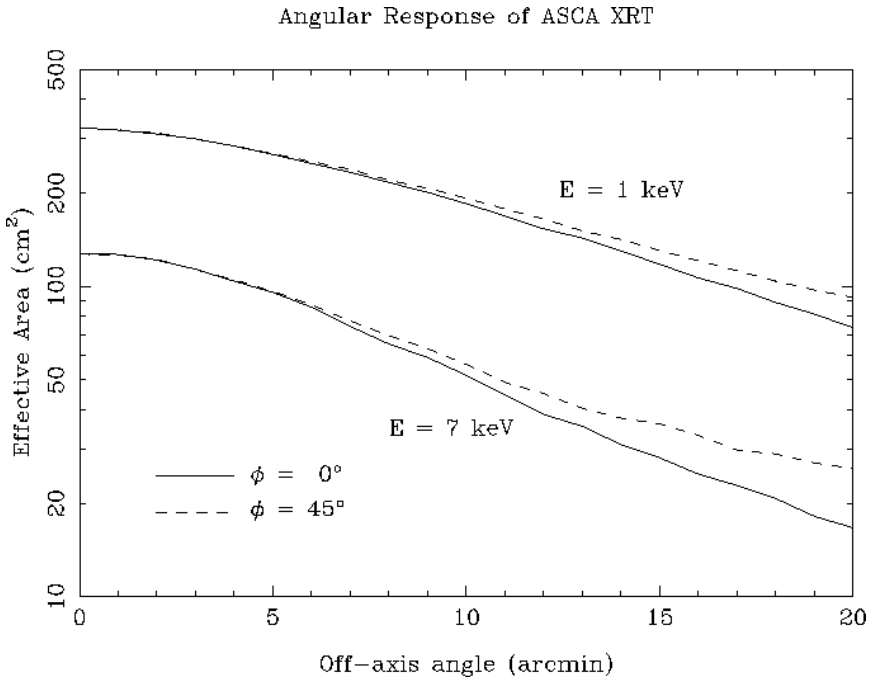

Figure 3.4: Effective area of a single XRT as a function of the off-axis angle. The data for incident X-rays of 1.0 and 7.0 keV are shown.

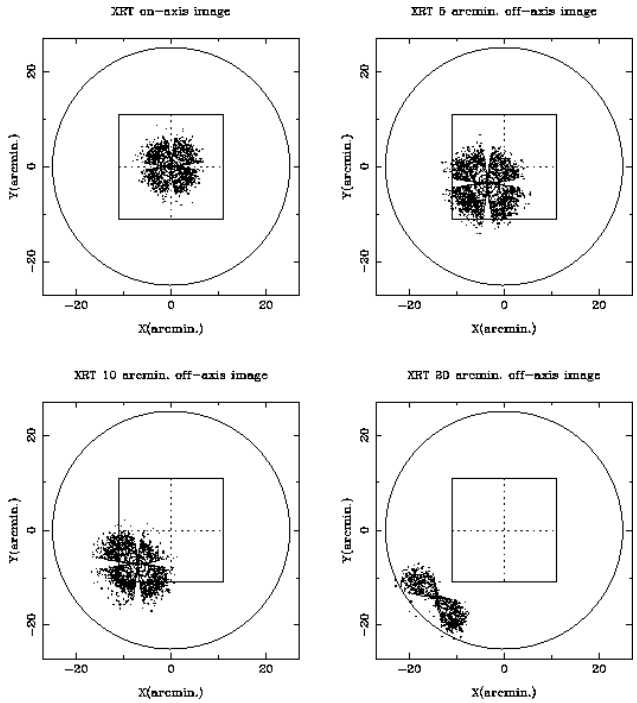

Figure 3.5: The point spread function of ASCA XRT.

several incident positions. The apparent butterfly-like structure is due to junctions between the four quadrants of each XRT. The half power diameter (HPD) is $\sim 3'$, and 80% of the incident energy is encircled in a $6'$ diameter for an on-axis source. Two point sources can be distinguished if the separation is over $\sim 30''$.

Stray light (photons from outside of the FOV) is another weak point of ASCA XRTs. It is caused by irregular manners of reflection, such as single or more than three reflections or reflections at the back side of the foils. Figure 3.6 shows the GIS image of the stray light from Crab nebula, which is located at 1° away from the center of GIS.

3.3 GIS: Gas Imaging Spectrometer

GISs (GIS2 and GIS3) are gas scintillation proportional counters, placed on the focal planes of XRTs. When compared with SIS, the characteristics of GIS are the larger FOV, higher sensitivity in the hard X-ray band and better timing resolution (see table 3.1 for basic properties of GIS).

Figure 3.7 shows the operating mechanism of GIS. An incident X-ray photon is detected by the gas mixture of Xe (96%) and He (4%), then a cloud of photo electrons is produced in the

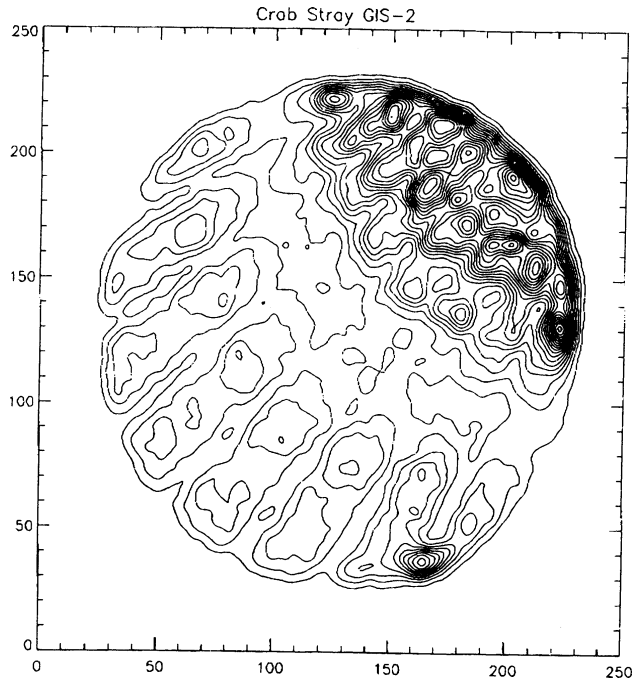

Figure 3.6: The stray light image obtained with GIS2. Crab nebula is at 1° from the center of GIS.

Table 3.1: Basic properties of GIS.

Size of one pixel	0.5 mm ($\simeq 0'.5$)
FOV (diameter)	$50'$
Energy band	0.7–10.0 keV
Energy resolution	8% at 5.9 keV (FWHM)
Timing resolution	62.5 ms for usual PH mode

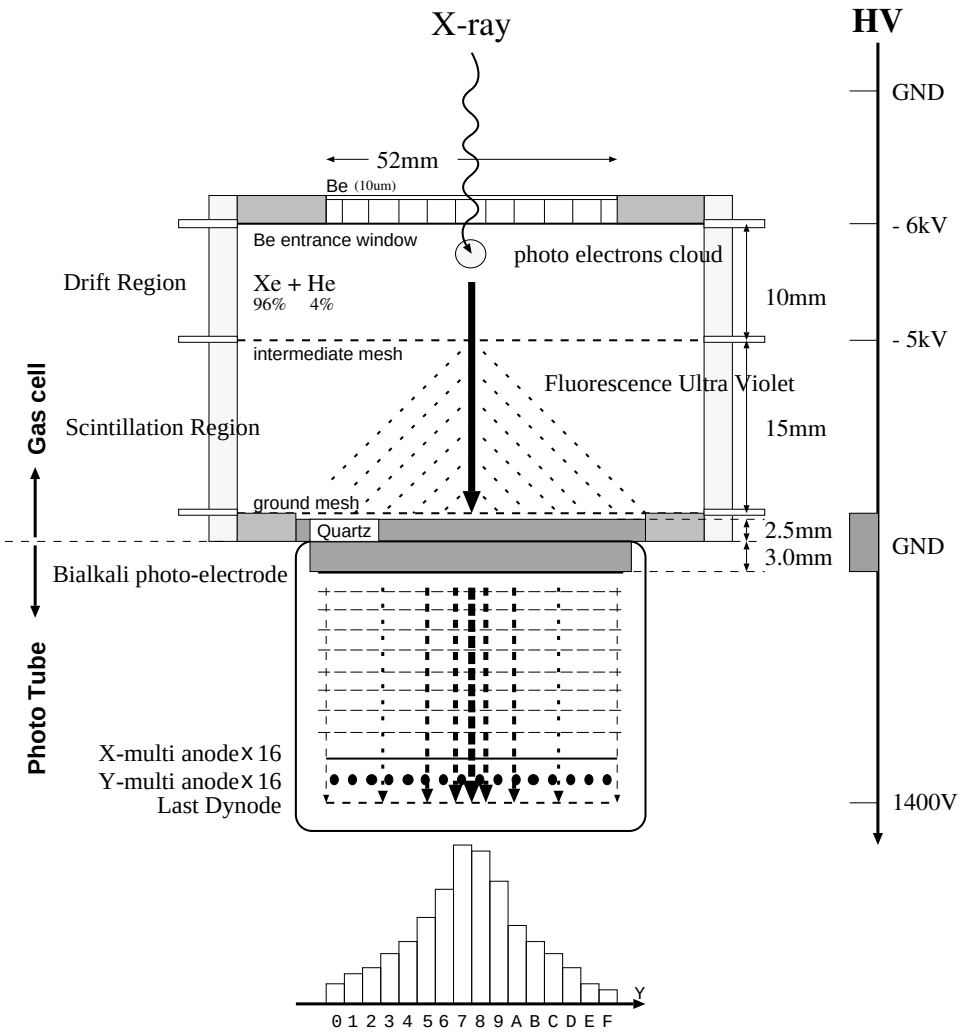

Figure 3.7: The schematic view of the operating mechanism of GIS.

drift region. The cloud is drifted by the weak electric field and enters the scintillation region. It is then accelerated by the strong electric field there, but Xe atoms are not ionized as in a gas proportional counter. Instead, they are excited by electrons with sufficient energy, and when they de-excite, UV photons are emitted. Therefore the number of UV photons is proportional to that of electrons in the cloud, hence to the energy of the incident photon. Finally the UV photons are detected by the the imaging phototube. The energy resolution (FWHM) is $\sim 8\%$ at 5.9keV and has dependence on the X-ray energy E as $E^{-0.5}$. The effective area of a single GIS combined with the XRT is shown in figure 3.8.

GIS has two observation modes: pulse height (PH) mode and multi-channel pulse count (MPC) mode. Normally PH mode is used. In this mode, 31 bits are assigned for the pulse

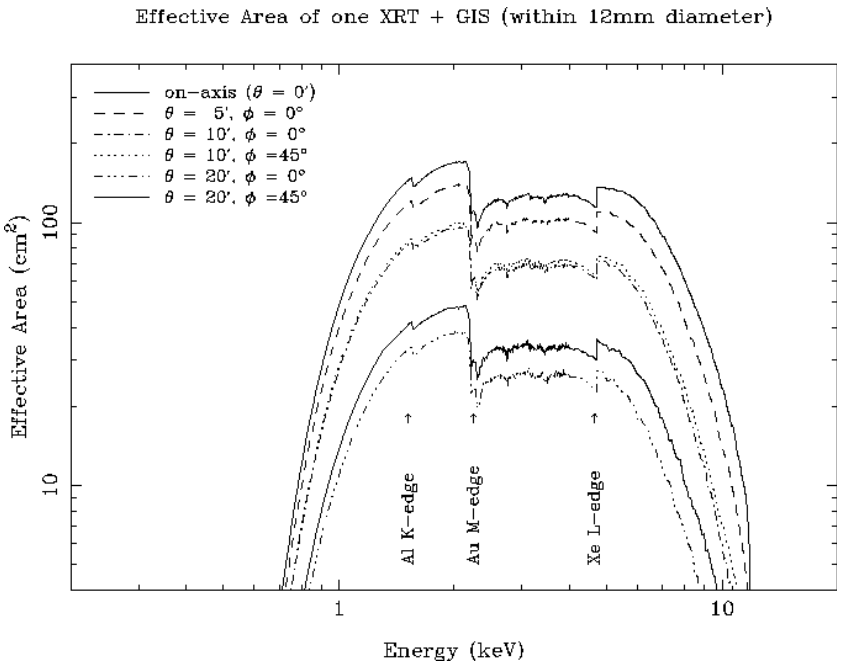

Figure 3.8: The energy dependence of the effective area of a single GIS, combined with the XRT. Dependence on the off-axis angle θ and azimuthal angle ϕ is also shown.

height (PH), X position (RAWX), Y position (RAWY), rise-time (RT), spread of UV photons (SP) and event time ("timing bit"), usually as 10, 8, 8, 5, 0, 0 bits, respectively. We can adjust the bit assignment within a limited degree of freedom as presented in table 3.2. MPC mode, which has been rarely used, is for bright sources. In this mode, positional information is not recorded. The timing resolution and maximum source intensity for various recording rate are summarized in table 3.3. The gain is always monitored with a radio isotope ^{55}Fe attached to each GIS, which emits monochromatic X-rays with an energy of 5.89 keV.

3.4 SIS: Solidstate Imaging Spectrometer

SISs (SIS0 and SIS1) are the first CCD cameras used for X-ray astronomy. As shown in figure 3.9, each SIS consists of four chips, called S0C0 (chip0 of SIS0), S0C1 (chip1 of SIS0), ... and S1C3 (chip3 of SIS1). When compared with GIS, the characteristics of SIS are the higher energy resolution, higher sensitivity in the soft X-ray band and better position resolution. Basic properties of SIS are given in table 3.4. The effective area of a single SIS combined with the XRT is shown in figure 3.10.

SIS has three observation modes: Faint, Bright and Fast mode. In the Faint mode, positional

Table 3.2: Freedom of bit assignment for PH mode of GIS.

	Possible number of bits assigned
PH	6, 8, 10*
RAWX	6, 8*
RAWY	6, 8*
RT	0, 5*, 6, 8
SP	0*, 8
Timing bit	0*–10
Total	31

*: Default assignments.

Table 3.3: The timing resolution and the maximum source intensity of GIS.

Mode	Bit rate	Timing resolution (sec)	Maximum source intensity
PH	H	0.0625*	256 count/sec
	M	0.5*	32 count/sec
	L	2.0*	8 count/sec
MPC	H	0.5	128 Crab†
	M	4.0	16 Crab†
	L	16.0	4 Crab†

†: 1 Crab corresponds to $\sim$ 1000 count/sec.
*: For the case when the timing bit is 0.

Table 3.4: Basic properties of SIS.

Size of one pixel	0.027 mm ($\simeq 0'.027$)
FOV	$11' \times 11'$ per one chip
Energy band	0.5–10.0 keV
Energy resolution	2% at 5.9 keV (FWHM)
Timing resolution	4/8/16 s for 1/2/4-CCD mode

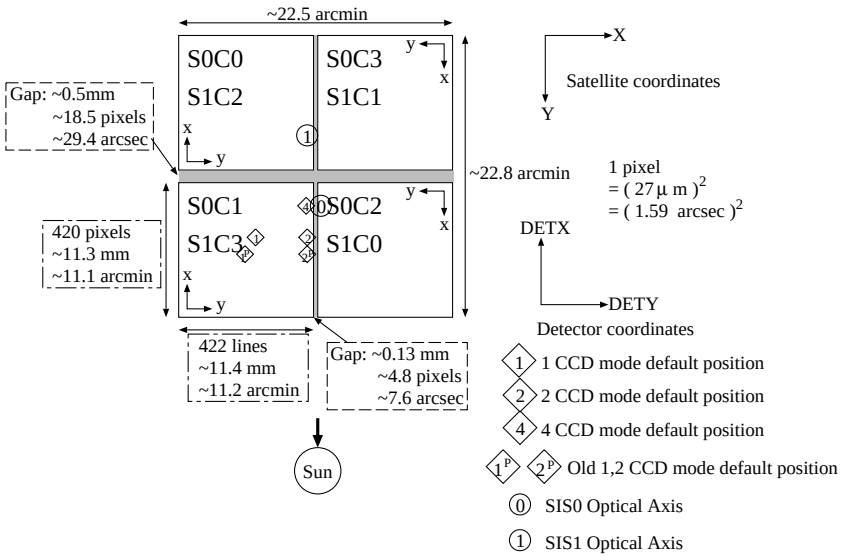

Figure 3.9: SIS chip configuration.

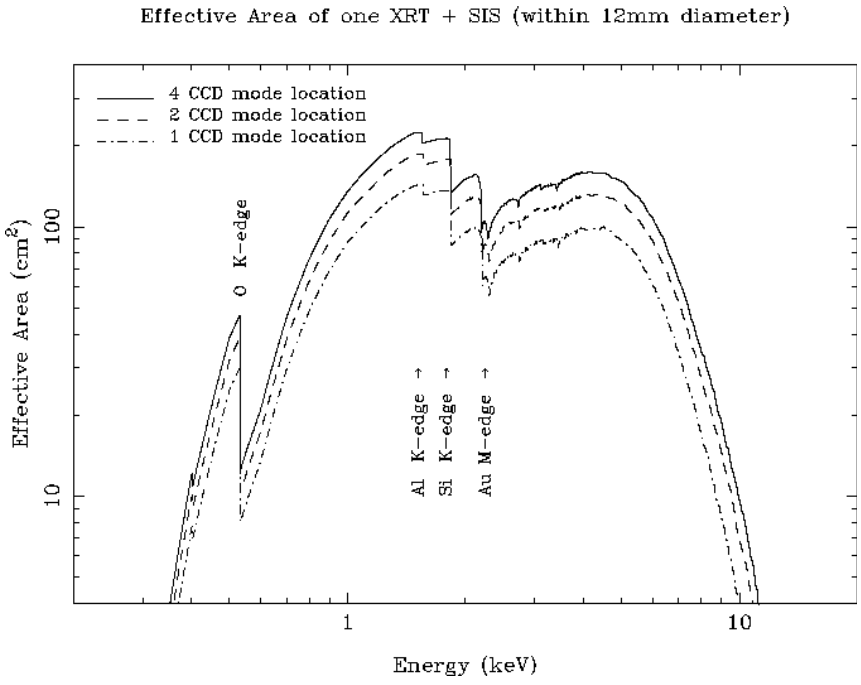

Figure 3.10: The energy dependence of the effective area of a single SIS, combined with the XRT. Dependence on the source locations is also shown.

Table 3.5: The timing resolution and the maximum source intensity of SIS.

Mode	Bit rate	Timing resolution (sec)	Maximum source intensity (count/sec)
Faint	H	4/8/16*	128
	M	4/8/16*	16
	L	4/8/16*	4
Bright	H	4/8/16*	512
	M	4/8/16*	64
	L	4/8/16*	16
Fast	H	0.016	1024
	M	0.016	128
	L	0.016	32

*: For the 1/2/4-CCD mode, respectively.

information of the center pixel[1] and the pulse-height of each 9 (3×3) pixels surrounding the center pixel are recorded as one event. In the Bright mode, each event is classified into eight grades (grade 0–7, see figure 3.11). The pulse heights are summed up according to the determined grade. Then the sum of pulse heights, the positional information of the center pixel, and the grade are recorded as one event. Usually, events of grade 0, 2, 3 and 4 are regarded as X-ray events. In these two modes, we can use 1, 2 or 4 chips of each SIS according to the scientific goal of the observation[2]. Timing resolution is determined by the time necessary to read out all the chips being used: 4 s per one chip (see table 3.5). The Fast mode is for very bright sources and operated with only one chip of each SIS. In this mode, better timing resolution of 16 ms is obtained at the expense of positional information.

The correction sequence of pixel dark levels is as follows. In orbit, the dark level averaged over each 16×16 pixels ("dark frame") is estimated by the onboard CPU and subtracted from the PH of each pixel. Dark Frame Error (DFE) is difference between the real average dark level and the dark frame. On the ground, DFE averaged over the whole chip is estimated using the PH values of corner pixels[3], and is subtracted again.

Only the "average" dark level is taken into account in these correction methods. Therefore difference between the dark level of each pixel and DFE-corrected PH value still exists. It is called Residual Dark Distribution (RDD). RDD is corrected by the RDD map, which possesses the information of the dark level of each pixel.

[1]Center pixel is a pixel where the pulse-height distribution is maximum among the surrounding 3×3 pixels.

[2]We use the terms like "1-CCD Faint mode" or "4-CCD Bright mode."

[3]Corner pixels are pixels on the corners of each 3×3 pixels around the center pixel.

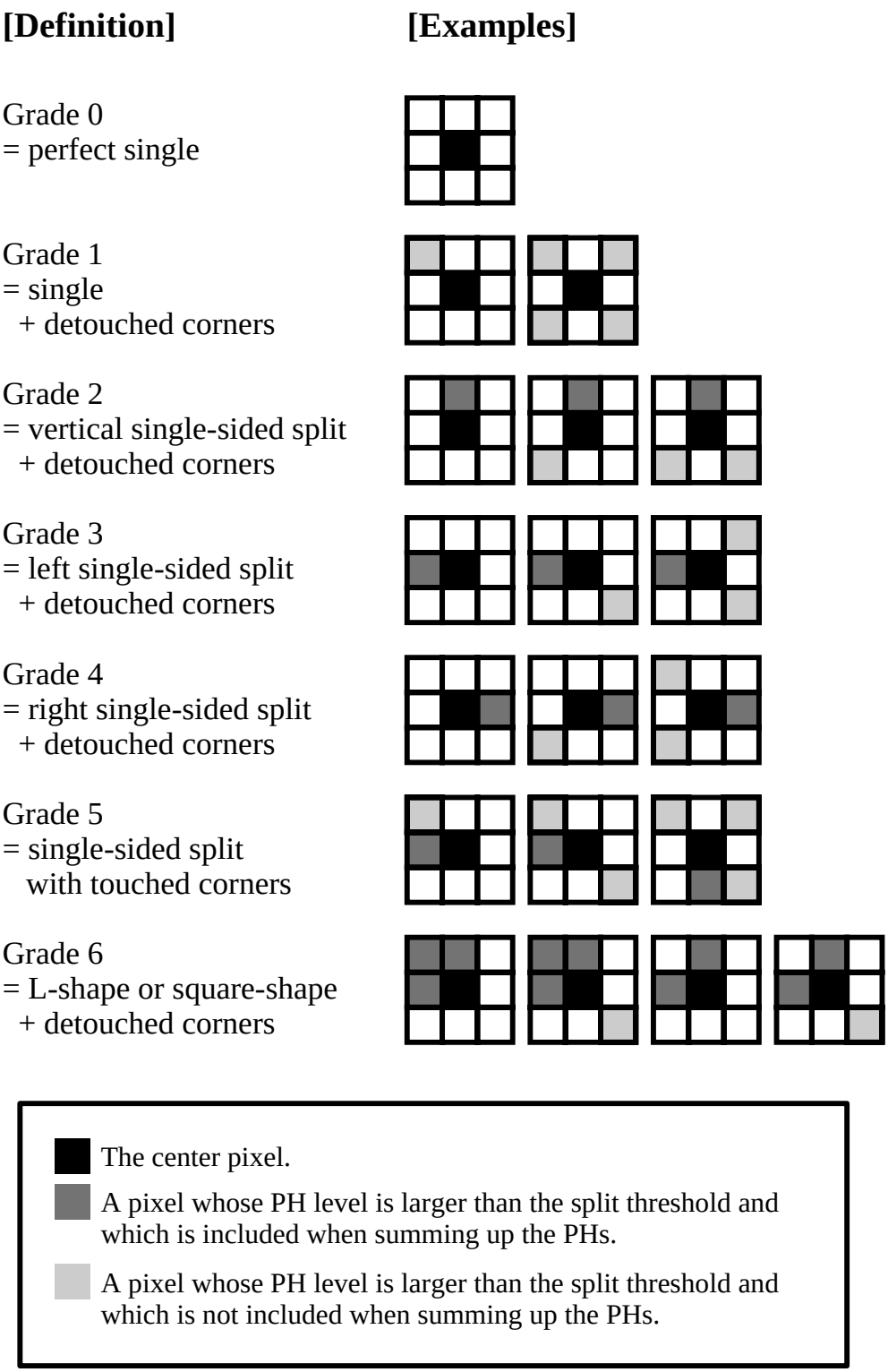

Figure 3.11: Grade definition (0–6) for one event of SIS. All the other patterns are classified as grade 7.

Pixels damaged by charged particles show various values of dark currents, according to the degree of damage. This fact is the main cause of RDD. Therefore the data taken in 4-CCD mode are more affected than those taken in 2/1-CCD mode because of the longer exposure time. In addition, later observations are more affected than earlier ones because the degree of damage has been increasing since the launch.

Chapter 4

Observations and Data Reduction

ASCA has observed the SMC for 10 times as of 1998. The data of eight observations were available (mostly archival data), and we used all of them. Observation dates, pointed directions and other relevant information are presented in table 4.1. Most of the optically bright portion and the Eastern Wing are already covered.

Table 4.1: SMC fields observed with ASCA and used in this paper.

Sequence Number	Observation Date	Target Name	Pointed Direction* R.A.	Dec.	Expos.† GIS/SIS	SIS‡ Mode
40005000	93/04/26	SMC X-1	$1^h17^m04^s$	$-73°26'34''$	4/—	—
50020000	93/05/12	E0102−72.2	$1^h04^m02^s$	$-72°01'55''$	35/31	1F
43024000	95/10/18	SMC X-1	$1^h17^m04^s$	$-73°26'35''$	41/—	—
54013000	96/05/21	0103−72.6 N1	$1^h04^m52^s$	$-72°23'11''$	42/33	1F
54013010	96/05/22	0103−72.6 N2	$1^h04^m52^s$	$-72°23'11''$	36/28	1F
55032000	97/11/13	N19	$0^h47^m16^s$	$-73°08'30''$	43/38	2F
55033000	97/11/14	N66	$0^h59^m25^s$	$-72°10'12''$	39/34	2F
15508000	97/12/12	SMC X-3	$0^h52^m06^s$	$-72°26'06''$	20/—	—
15609000	98/11/18	XTE J0111.2−7317	$1^h11^m26^s$	$-73°25'07''$	26/—	—

*: Equatorial coordinates (J2000). †: Available exposure time in ksec. ‡: "1/2F" represent 1/2-CCD Faint mode.

In each observation, X-ray photons were collected with four XRTs and detected separately with two GISs and two SISs. We screened the obtained data with normal criteria: e.g. rejected the data obtained in SAA (South Atlantic Anomaly), or when the cut-off rigidity was lower than 4 GeV/c, or when the elevation angle was lower than 5°. For GIS, we also rejected the particle events with a rise time discrimination method. For SIS, the data obtained when the elevation angle from the bright earth was lower than 25° were also rejected. The effects of RDD were corrected if the observation was carried out later than 1996. After the screening, total available exposure time of two GISs was $\sim$ 570 ks.

Chapter 5

Results

5.1 X-ray images

5.1.1 Images and source extraction

We created X-ray images in the soft (0.7–2.0 keV) and hard band (2.0–7.0 keV) for each observation. X-ray sources were extracted from the images, according to the criterion that S/N ratio of photon counts in any circle with $3'$ radius should exceed 5. In some source-crowded areas, we used a circle with smaller radius ($1'.5$–$2'$) to lessen the contamination of nearby sources. Consequently 39 sources were extracted, which are presented at the end of this chapter (table 5.18). Counterparts of each source in X-ray and radio band were identified within a circle of $1'.5$ radius centered on the source.

Two sources No. 4 and No. 5 were separated by only $2'$, hence we could not derive a reliable value of S/N ratio for each of them (only 30% of incident photons are encircled in a circle with $1'$ radius). However, S/N ratio of photon counts in a circle containing both of them exceeded 5. In addition, No. 4 looked more prominent in the soft band while No. 5 in the hard band. These facts indicate that there really exist two sources and that No. 4 is a softer source while No. 5 is a harder source. S/N ratio of No. 34 exceeded 5 in the hard band, while in the soft band it suffered the severe contamination from No. 30.

Mosaic images made from these observations are shown in figure 5.1. Among the two observations centered on SMC X-1, only one (observed in 1995) was used. Soft band images have been reported with Einstein and ROSAT (WW92; K99). However, our soft band image is different from previous ones, reflecting variabilities of the SMC X-ray sources. The hard band image is obtained for the first time and is significantly different from the soft band one.

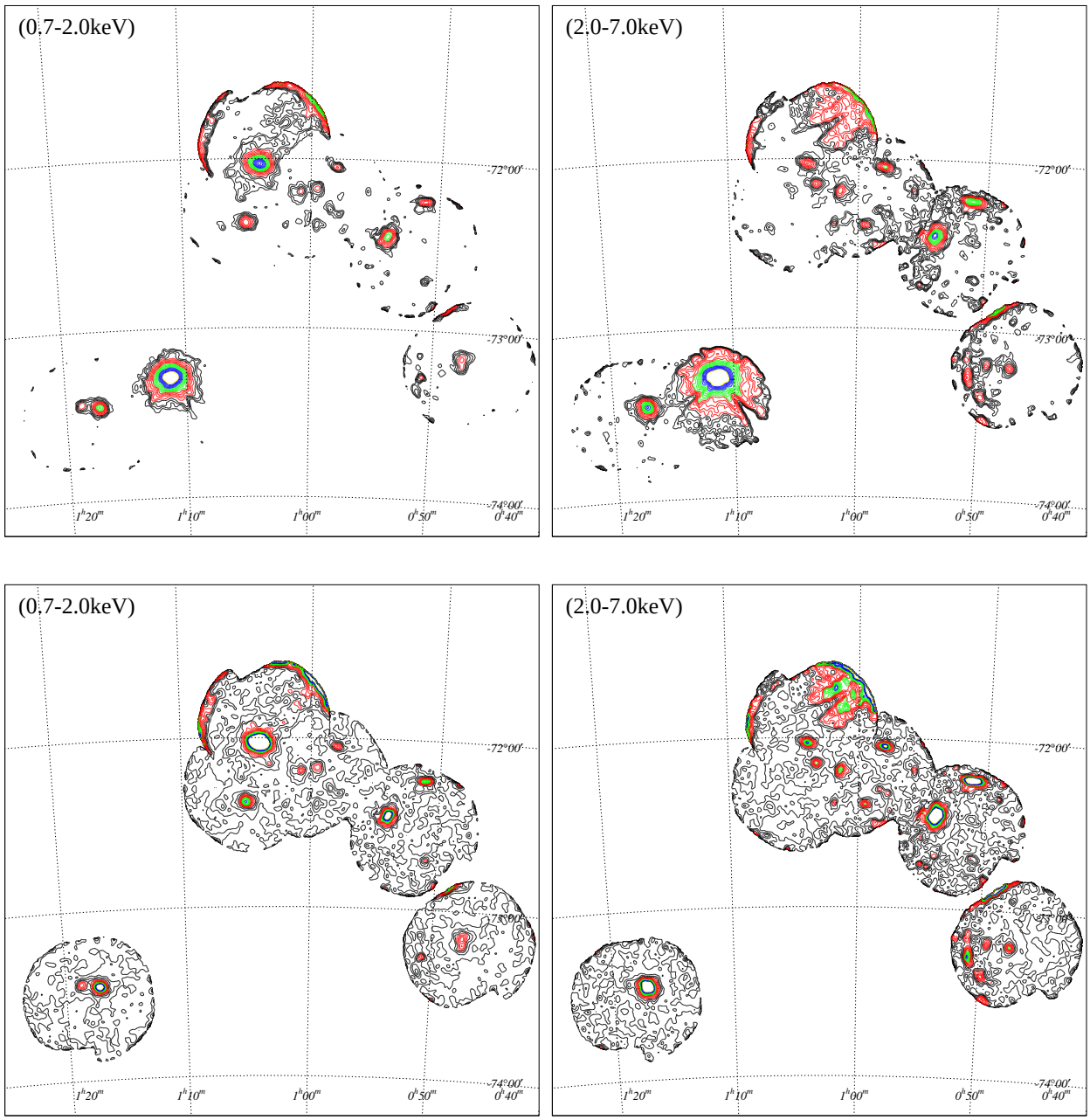

Figure 5.1: SMC mosaic contour images obtained with ASCA GIS in the soft (0.7–2.0 keV; left panels) and hard band (2.0–7.0 keV; right panels), overlaid with the equatorial coordinates (J2000). The effects of non X-ray background, telescope vignetting and difference of exposure time between observations were corrected. The complex structure for sources near the edge of the detector fields is due to the point spread function of ASCA XRTs. In the upper panels, contour levels are logarithmically spaced and highly saturated at XTE J0111.2−7317. In the lower panels, the field of XTE J0111.2−7317 is omitted and contour levels are linearly spaced.

5.1.2 Definition of the hardness ratio

We defined the hardness ratio (HR) for each source as follows.

1. The source region was taken as a circle or an ellipse with dimensions of $\sim 2'$–$6'$ centered on the source. The eccentricity was taken to be larger if the source was located at larger off-axis angle because of the distortion of the point spread function (figure 3.5).

2. The background region was taken from nearby off-source areas.

3. We derived the photon counts from the respective regions in the soft (0.7–2.0 keV) and hard band (2.0–7.0 keV). Then HR was defined as

$$\mathrm{HR} \equiv \frac{H - S}{H + S}, \tag{5.1}$$

where H and S are GIS photon counts after background subtraction in the hard and soft band, respectively. We could not define HR for No. 4, No. 5 and No. 34, due to the contamination described in the previous subsection. According to the definition, the value of HR ranges from -1 to 1, and is larger for a harder source.

Figure 5.2 shows the plot of HR as a function of the detected (raw) count rate in 0.7–7.0 keV. If a source was detected in multiple observations, its HR and count rate were derived from each observation. We should note that the difference of count rate between two sources does not necessarily indicate the difference of the intensity, because the count rate is affected by the vignetting of XRTs as shown in figure 3.4. We can see that in higher count rate region (count rate $\gtrsim 0.005$), there exists a split between harder and softer sources.

5.2 Timing analyses

We performed the FFT (Fast Fourier Transform) analysis on all the sources to search for coherent pulsations. For some sources with high count rate, we used only high-bit data to obtain a better time resolution of 62.5 ms. For the remaining sources, we used high-bit and medium-bit data simultaneously to get better photon statistics. The resultant time resolution was 1 s. We have detected coherent pulsations from 11 sources. Five of them were first discovered during this analysis, while the others were confirmations of previous discoveries. See figure 5.4 and table 5.1 for the history of discoveries.

To search for coherent pulsations from the source No. 5=AX J0049$-$732, we made an event list extracted from a circle with $3'$ radius centered on AX J0049$-$732, and performed the FFT

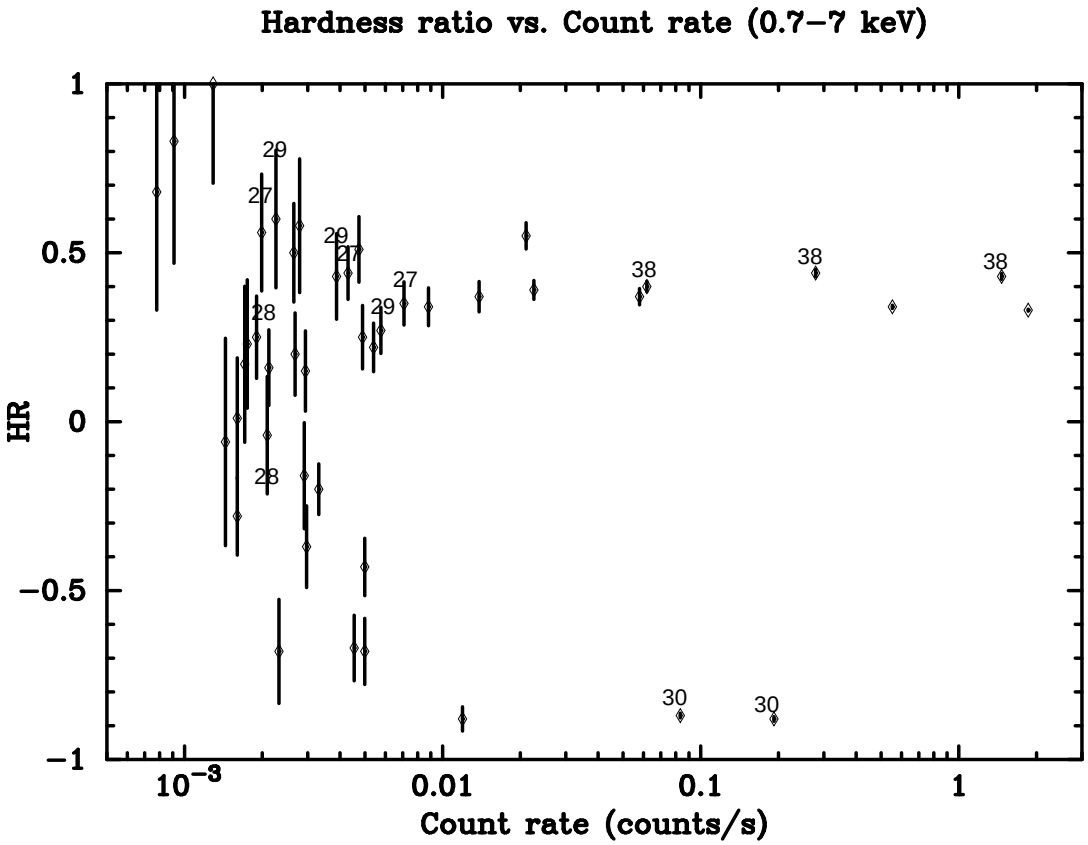

Figure 5.2: The plot of HR as a function of the detected (raw) count rate of GIS in 0.7–7.0 keV. Error bars of HRs indicate the statistical errors. The sources which were detected multiple times are marked with the source number.

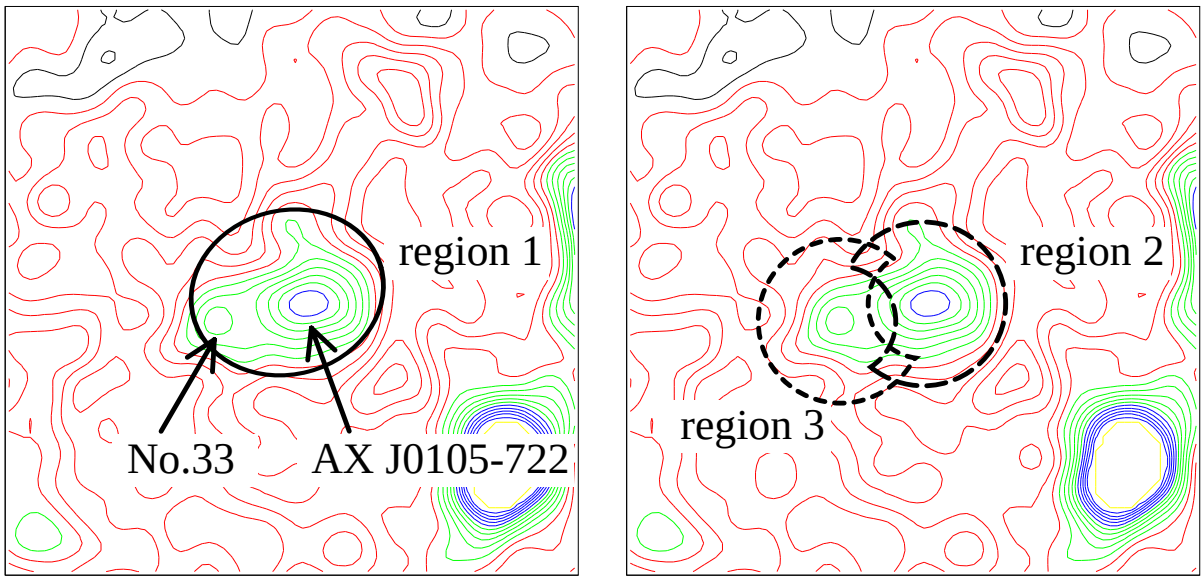

Figure 5.3: X-ray contours obtained with GIS overlaid with the three regions from which event lists were extracted to search for coherent pulsations from AX J0105−722.

analysis on the light curve. Coherent pulsations of 9.1321 s period were discovered with a 99.98% significance (Imanishi, Yokogawa & Koyama 1998). However, as noted in subsection 5.1.1, separation between AX J0049−732 and the source No. 4 (SNR 0047−735) is only $\sim 2'$. Therefore the detected pulsations might be attributed to the SNR. In order to check this point, we also performed the FFT analysis on the events extracted from a circle with $3'$ radius centered on the SNR, and detected no sign of pulsations. Hence we concluded that the pulsations could be attributed to AX J0049−732, not to the SNR. Separation between two sources No. 32=AX J0105−722 and No. 33 is only $\sim 3'$. Coherent pulsations of 3.34300 s period were discovered with a significance of $\sim 99.5\%$ (Yokogawa & Koyama 1998c) from an event list extracted from an oval-shaped region which included both of AX J0105−722 and No. 33 (region 1 in figure 5.3). We also extracted event lists from the regions 2 and 3, shown in figure 5.3. The event list extracted from region 2 showed weak evidence of 3.34300 s period, while that from region 3 did not. Therefore we concluded the pulsating source was AX J0105−722, not No. 33, though the significance of pulse detection is not so high.

For the 11 sources from which pulsations were detected by the FFT analysis, we performed the epoch folding search to determine more precise pulse periods, which are presented in table 5.1. In addition, we did it for previously known pulsars XTE J0055−724 (No. 16), SMC X-1 (No. 38; observed in 1995) and RX J0052.1−7319 (No. 14), from which we could not detect

coherent pulsations by the FFT analysis. Since SMC X-1 was in the 0.6 day eclipse phase, we extracted an event list from non-eclipse time. We then found weak peaks near the known periods for the former two sources (χ^2/d.o.f. was 22.40/7 for XTE J0055−724 and 39.71/7 for SMC X-1). Wojdowski et al. (1998) report that they did not detect coherent pulsations in the same data of SMC X-1. We could not detect any sign of coherent pulsations from RX J0052.1−7319.

Since the orbital elements and the ephemeris of SMC X-1 system is well known, we corrected for the Doppler effect on the pulse period. We adopted the orbital elements in Wojdowski et al. (1998). Since the eccentricity is near zero (< 0.00004), the intrinsic period p_0 was derived as

$$p_0 = \frac{p}{1 - 2\pi a \sin i \sin \Phi / c P_{\rm orb}}, \tag{5.2}$$

where p, a, i, Φ and $P_{\rm orb}$ are the pulse period determined by the epoch folding search, radius of the orbit, inclination angle, orbital phase at the midst of the observation, and orbital period, respectively. Thus derived periods are presented in table 5.1.

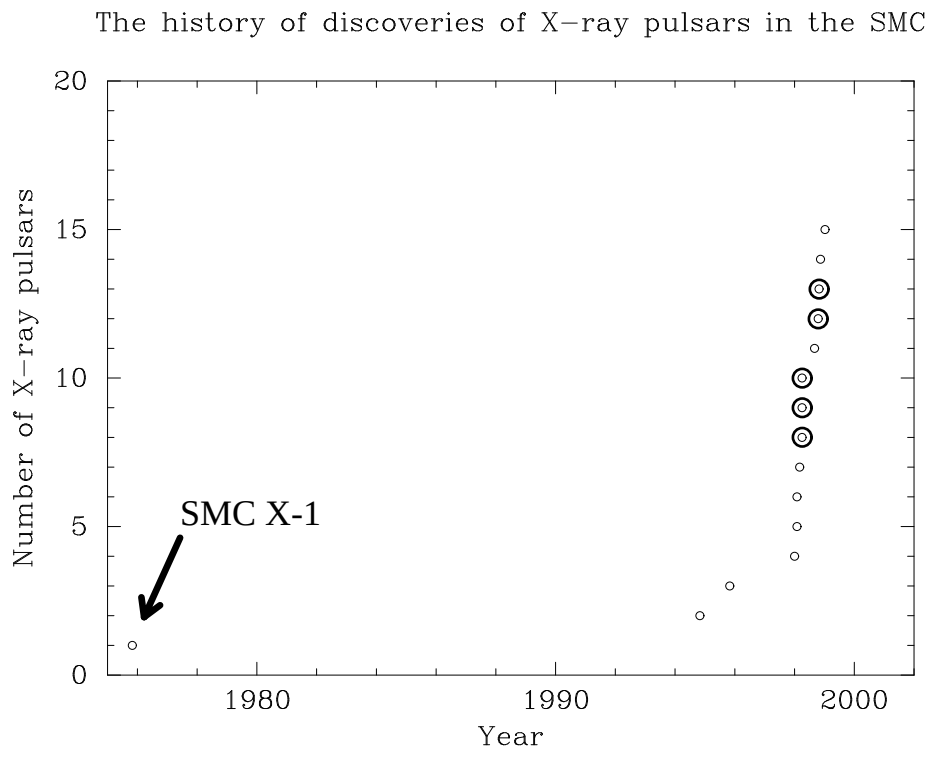

Figure 5.4: The history of discoveries of X-ray pulsars in the SMC. Our discoveries are marked with double circles.

Table 5.1: X-ray pulsars in the SMC.

No.	Name	Discovery			[This work]	Refs.
		Year	Satellite	Period (s)	Period (s)	
38	SMC X-1‡	1976	(Rocket)	0.716	0.70865(6)^{a*} 0.7100(5)^{b*} 0.7065(5)^{c}	[1][2]
25	RX J0059.2−7138‡	1994	ROSAT	2.7632	2.7632(3)	[2][3]
—	2E 0050.1−7247‡	1995	ROSAT	8.8816	—	[2][4]
15	AX J0051−722	1997	RXTE, ASCA	91.12	91.1(1)	[5][6]
11	1WGA J0053.8−7226‡		ASCA	46.63	46.63(2)	[5][7]
—	XTE J0054−720	1998	RXTE	169.3	—	[6][8]
16	XTE J0055−724‡		RXTE, BeppoSAX	58.97	59.00(2)	[9][10]
3	AX J0049−729*		RXTE, ASCA	74.68	74.68(3)	[5][11]
8	AX J0051−733*‡		ASCA	323.2	323.2(5)	[8][12][13][14]
20	AX J0058−720*		ASCA	280.4	280.4(4)	[12]
29	1SAX J0103.2−7209‡		BeppoSAX	345.2	348.9(3)	[10][15][16][17]
32	AX J0105−722*†		ASCA	3.34300	3.34300(3)	[18]
5	AX J0049−732*		ASCA	9.1321	9.1321(4)	[19]
37	XTE J0111.2−7317‡		RXTE, CGRO	31	30.9497(6)	[20][21][22]
14	RX J0052.1−7319‡	1999	ROSAT	15.3	—	[22][23]

Notes: Columns 3–5 give the year of discovery, the satellite which discovered the pulsations and the pulse period at that time. Column 6 gives the period determined in this work with ASCA data. Possible maximum errors in the last digits are given in the parentheses. Correction of the Doppler effect was performed only for SMC X-1. *: First discovered during this work. †: Significance of pulse detection is $\sim 99.5\%$. ‡: Optically identified with a B star (SMC X-1), a blue star (RX J0059.2−7138) or a Be star (the others). [a–c]: SMC X-1 was detected three times: in 1993[a], 1995[b] and 1998[c]. *: Wojdowski et al. (1998) report that the period was 0.7086390(9) s in the 1993 observation and was not detected from the data of 1995.

References: [1] Lucke et al. 1976, [2] Bildsten et al. 1997, [3] Hughes 1994, [4] Israel et al. 1997, [5] Corbet et al. 1997, [6] Lochner et al. 1998, [7] Buckley et al. 1997, [8] Cowley et al. 1997, [9] Marshall & Lochner 1998; Santangelo et al. 1998, [10] Israel et al. 1998, [11] Yokogawa & Koyama 1998a, [12] Yokogawa & Koyama 1998b, [13] Cook 1998, [14] Schmidtke & Cowley 1998, [15] Yokogawa & Koyama 1998d, [16] Hughes & Smith 1994, [17] Ye et al. 1995, [18] Yokogawa & Koyama 1998c, [19] Imanishi, Yokogawa & Koyama 1998, [20] Chakrabarty et al. 1998a; Wilson & Finger 1998, [21] Chakrabarty et al. 1998b, [22] Israel et al. 1999, [23] Lamb et al. 1999.

We also searched for burst-like activities by using light curves binned with various time scales from $\sim$ second to $\sim$ hour. However, no prominent burst was found.

5.3 Spectral analyses

In this section, we present the results of spectral fitting of each source with some models. Derived parameters (photon index Γ, temperature kT and column density $N_{\rm H}$), fluxes ($F_{\rm x}$) and absorption-corrected luminosities ($L_{\rm x}$) are presented in table 5.18. Source and background regions were taken as the same as those taken when we defined HR in subsection 5.1.2. We did not analyze the spectra of No. 4 (SNR 0047−735), No. 5 (X-ray pulsar AX J0049−732) and No. 34 because of the contamination (see subsection 5.1.1).

No. 27, No. 28 and No. 29 (1SAX J0103.2−7209) have been detected multiple times. Spectral parameters and flux derived in each observation were consistent with each other for the respective sources. Therefore, to obtain a better constraint on the parameters, we combined the multiple spectra into one and fit it again. No. 38 (SMC X-1) has been also detected multiple times. Since it showed a large-scale flux variability, we did not combine the spectra. The SNR 0102−723 (No. 30) has been detected twice in the GIS field (in 1993 and 1996) and only once in the SIS field (in 1993). Here we used only the SIS spectrum (subsection 5.3.2).

5.3.1 X-ray pulsars and HMXBs

As summarized in table 5.1, we detected 13 X-ray pulsars. In addition, No. 22 and No. 13 are positionally coincident with RX J0058.2−7231 and RX J0051.9−7311, both of which are HMXBs with a Be star companion (Cowley et al. 1997; Schmidtke et al. 1998). X-ray spectra of these classes are basically described by an absorbed power-law below $\sim$ 10 keV, hence we adopted it for the spectral fitting.

We used only GIS2 spectrum for AX J0051−733 (No. 8), RX J0059.2−7138 (No. 25), SMC X-1 (observed in 1998) and RX J0051.9−7311, because RX J0059.2−7138 was detected only on the edge of GIS2 and the other three were detected near the calibration source of GIS3. Otherwise we added the spectra of GIS2 and GIS3 to obtain better statistics.

The simple power-law model showed a soft excess for three sources RX J0059.2−7138, XTE J0111.2−7317 (No. 37) and SMC X-1 (in each observation). Introducing a blackbody as the soft component gave a better fit. Spectral parameters, fluxes and absorption-corrected luminosities in table 5.18 are derived from this two-component model for these sources.

The spectra and best-fit models of the pulsars are given in section 5.4, together with other relevant information.

5.3.2 SNRs

We detected eight radio SNRs, i.e. 0102−723 (No. 30), 0103−726 (No. 31), N19 (No. 1), N66 (No. 24), DEM S128 (No. 32[1]), 0056−725 (No. 21), 0049−736 (No. 12) and 0047−735 (No. 4[2]). Before fitting their spectra, we extracted thermal SNRs (SNRs emitting thermal X-rays) from them. The direct clue to distinguish thermal spectra from non-thermal ones is the existence of emission lines of highly ionized atoms. The brightest SNR 0102−723 exhibits such a sprctrum, hence is undoubtedly a thermal SNR (e.g. Hayashi et al. 1994). We examined the existence of emission lines in the spectra of the other SNRs as follows.

1. To obtain a better energy resolution, we extracted the SIS spectra of 0103−726, N19 and N66. DEM S128 was out of the SIS fields, hence the GIS spectra were used instead. The other SNRs 0049−736 and 0056−725 were also detected only with GIS. However, we could not apply the following analysis to them because their spectra had very poor statistics.

2. We fitted the spectra in a narrow energy band ($\sim$ 1.1–3 keV) by a bremsstrahlung and three Gaussians with absorption. Center energies of the Gaussians were fixed to be 1.34 keV, 1.85 keV and 2.46 keV, representing the K_α lines from He-like Mg, Si and S, respectively.

3. We derived equivalent widths (EWs) and 90% confidence errors (δEWs) of the Gaussians. If EW was found to be greater than δEW for at least one Gaussian, i.e. if the SNR was found to exhibit an emission line from ionized atoms, we regarded it as a thermal SNR.

In this way, if an SNR which emits thermal X-rays had poor photon statistics, it would not be classified as a thermal SNR. Hence this classification criterion is rather conservative. The results are shown in table 5.2. Now we have four thermal SNRs while the remaining three are not classified.

We fitted the SIS spectra of thermal SNRs with thin-thermal plasma models as follows.

[1]No. 32=DEM S128 (radio SNR)=AX J0105−722 (X-ray pulsar)

[2]Excluded from the spectral analysis because of the contamination (subsection 5.1.1).

Table 5.2: The results of the analysis of line intensities in the SNR spectra.

No.	Name	EW−δEW (eV) — Gaussian center (keV) — 1.34	1.85	2.46	Thermal or not
30	0102−723	—	—	—	Thermal*
31	0103−726	140 − 40	400 − 180	2000 − 1300	Thermal
1	N19	93 − 56	130 − 130	330 − 330	Thermal
24	N66	49 − 49	310 − 280	270 − 270	Thermal
32	DEM S128	40 − 40	0	320 − 320	—

*: Hayashi et al. (1994).

No. 30: 0102−723 The SIS spectrum of this SNR has been already intensively analyzed by Hayashi et al. (1994). We followed their model and determined its flux and absorption-corrected luminosity: $F_{\rm x} = 1.4 \times 10^{-11}$ erg s^{-1} cm^{-2} and $L_{\rm x} = 7.2 \times 10^{36}$ erg s^{-1} (0.7–10.0 keV).

No. 31: 0103−726 There are evident emission lines in the spectrum. Therefore we first adopted an absorbed thin-thermal plasma model (Raymond & Smith 1977), in which the condition of collisional ionization equilibrium (CIE) is assumed. The abundances of O, Ne, Mg, Si and S were treated as free parameters, while those of the other elements were fixed to be 0.2 solar, i.e. those in the interstellar matter in the SMC (Russell & Dopita 1992). The best-fit parameters and the model spectrum are given in table 5.3 and figure 5.5, respectively. Although the CIE model could reproduce the line profile fairly well, it was statistically rejected with 99% confidence.

We then included the effect of non-equilibrium ionization (NEI) in the plasma model (Masai 1994). An extra parameter, ionization timescale τ, was introduced. It is given as

$$\tau = \int_0^{\rm age} n dt, \tag{5.3}$$

where n is the electron density at time t ($t = 0$ corresponds to the time when the matter was shocked). If $\log \tau({\rm s\ cm^{-3}}) \gtrsim 12$, the plasma is in the CIE condition. The best-fit parameters and the model spectrum are given in table 5.3 and figure 5.5, respectively. It was also statistically rejected with 99% confidence. The larger χ^2 is due to the difference between the CIE/NEI plasma codes. The best-fit value of the ionization timescale indicates that the plasma of 0103−726 is in the NEI condition. However, the confidence contours shown in figure 5.6 suggest that we can not distinguish between a high temperature NEI plasma and a low temperature CIE plasma.

Table 5.3: Best-fit parameters of 0103−726 for the CIE or NEI model. Parentheses show the 90% confidence limits. Fluxes and absorption-corrected luminosities are derived from 0.7–10.0 keV band.

Model	$\log \tau$ (s cm^{-3})	kT (keV)	$N_{\rm H}$ (10^{21} H cm^{-2})	$F_{\rm x}$ (erg s^{-1} cm^{-2})	$L_{\rm x}$ (erg s^{-1})
CIE	—	0.37	0	1.1×10^{-12}	4.7×10^{35}
	—	(0.32–0.38)	(< 1)		
NEI	10.4	1.0	0	1.1×10^{-12}	4.7×10^{35}
	(10.3–10.6)	(0.8–1.1)	(< 0.1)		

Model	Abundances (solar)					χ^2/d.o.f.
	O	Ne	Mg	Si	S	
CIE	1.5	2.2	2.1	2.1	16	129.5/72
	(1.3–1.8)	(1.7–2.6)	(1.5–2.5)	(1.2–2.9)	(12–24)	
NEI	0.36	1.2	1.1	0.4	1.7	146.0/71
	(0.30–0.42)	(1.0–1.4)	(0.9–1.4)	(0.2–0.6)	(0.7–2.9)	

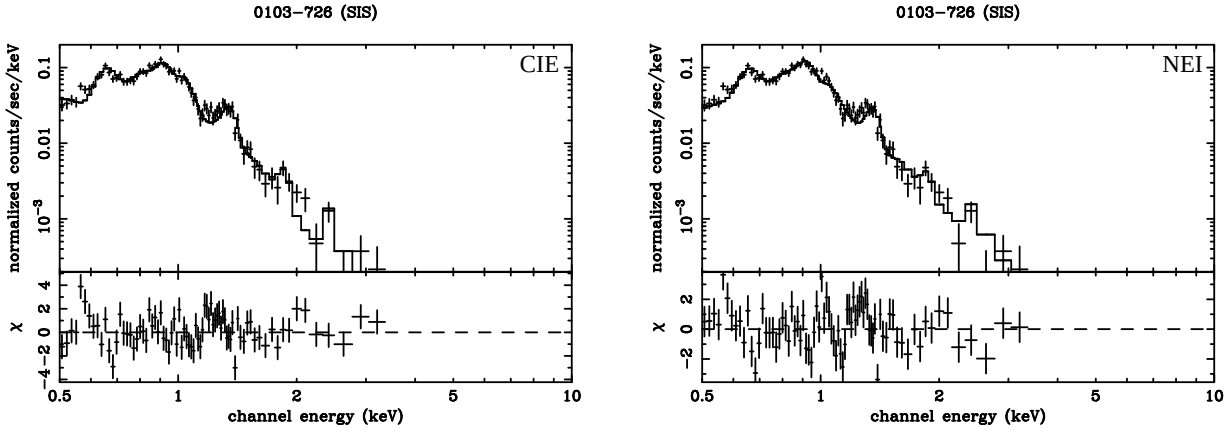

Figure 5.5: SIS spectra of 0103−726. Crosses and solid lines represent the observed data and the best-fit models (CIE on the left and NEI on the right), respectively.

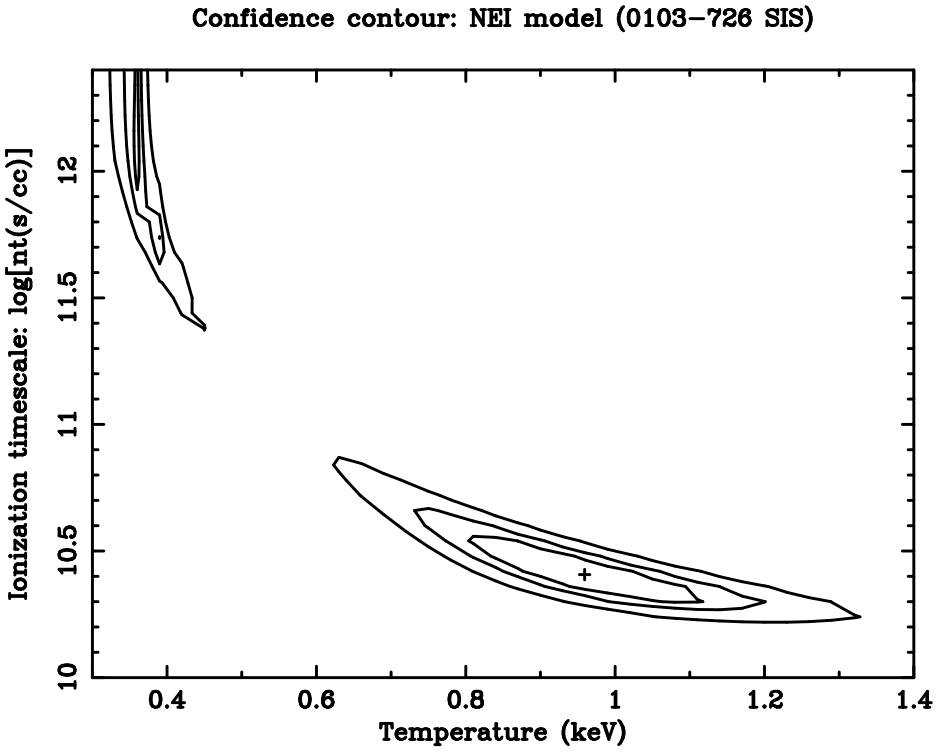

Figure 5.6: Confidence contours between the temperature and ionization timescale in the NEI model. Contours corresponds to 68%, 90% and 99% levels, respectively. Best-fit parameters are indicated by a plus sign.

No. 1: N19 The spectrum showed apparent emission lines of He-like Ne and Mg. Therefore we adopted an absorbed thin-thermal plasma model (CIE) and set the abundances of Ne and Mg to be free. Abundances of the other elements were fixed to be 0.2 solar. The results are given in table 5.4 and figure 5.7.

No. 24: N66 An absorbed thin-thermal CIE plasma model where the abundances of all elements were set to be 0.2 solar could well reproduce the SIS spectrum. The results are given in table 5.4 and figure 5.7.

Table 5.4: Best-fit parameters of N19 and N66 for the CIE model. Parentheses show the 90% confidence limits. Fluxes and absorption-corrected luminosities are derived from 0.7–10.0 keV band.

	kT	Abundances (solar)		$N_{\rm H}$	$F_{\rm x}$	$L_{\rm x}$	χ^2/d.o.f.
	(keV)	Ne	Mg	(10^{21} H cm^{-2})	(erg s^{-1} cm^{-2})	(erg s^{-1})	
N19	0.7	0.7	1.0	4	3.5×10^{-13}	3.9×10^{35}	19.05/34
	(0.6–0.8)	(0.3–1.8)	(0.3–1.8)	(3–6)			
N66	0.7	0.2	0.2	4	3.5×10^{-13}	3.9×10^{35}	23.32/23
	(0.6–0.8)	(fixed)	(fixed)	(2–5)			

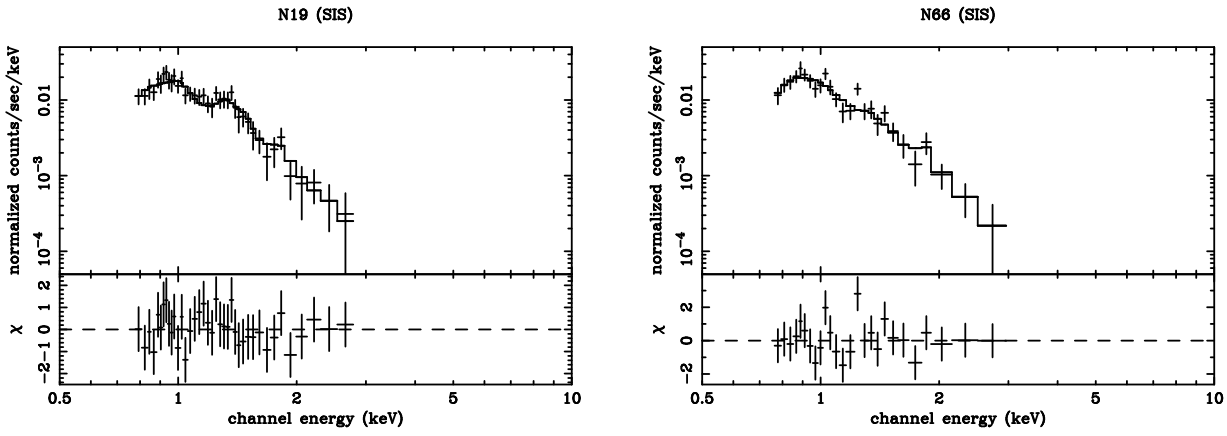

Figure 5.7: SIS spectra of N19 and N66. Crosses and solid lines represent the observed data and the best-fit CIE models, respectively.

For the unclassified SNRs, we adopted both of a thin-thermal CIE plasma model with absorption and an absorbed power-law model. Since their GIS spectra[3] had poor photon statistics, we fixed the global abundance to be 0.2 solar when the plasma model was applied. Their spectra were well fitted by both models (table 5.5). Specific details about these sources are given below.

No. 12: 0049−736 The spectrum was extracted only from GIS2 because this SNR was detected near the calibration source of GIS3. The derived temperature 0.7 keV is reasonable for an SNR. Therefore 0049−736 may be a thermal SNR.

No. 21: 0056−725 The derived temperature 20 keV is too high for an SNR, hence we adopted the power-law model in figure 5.8 and table 5.18. It may be implied that the spectrum of 0056−725 is really non-thermal.

No. 32: DEM S128 The derived temperature 3.2 keV may be reasonable if this SNR is very young. However, generally such a young SNR exhibits prominent emission lines which originate from the shock-heated ejecta. The fact that no emission line was identified prefers the power-law model, which is adopted in figure 5.8 and table 5.18. These facts imply the non-thermal nature of DEM S128. In addition, we have detected the evidence of pulsations from this source (= AX J0105−722) with a significance of 99.5%. The nature of DEM S128 is discussed in subsection 5.4.12.

5.3.3 The other sources

Since classes of most of the other sources are not well known and their spectra have poor photon statistics, it was unclear which model should be applied. Nevertheless, we adopted the power-law model to obtain rough estimation of their spectral parameters, fluxes and luminosities.

[3]They were detected out of the SIS fields.

Table 5.5: Best-fit parameters of 0049−736, 0056−725 and DEM S128. Parentheses show the 90% confidence limits. Fluxes and absorption-corrected luminosities are derived from 0.7–10.0 keV band.

Thin-thermal CIE plasma model

	kT (keV)	$N_{\rm H}$ (10^{21} H cm^{-2})	$F_{\rm x}$ (erg s^{-1} cm^{-2})	$L_{\rm x}$ (erg s^{-1})	χ^2/d.o.f.
0049−736	0.7	0.02	6.4×10^{-13}	2.8×10^{35}	3.656/5
	(0.3–1.0)	(< 5)			
0056−725	20	1	3.3×10^{-13}	1.5×10^{35}	5.001/5
	(> 4)	(< 9)			
DEM S128	3.2	0	2.9×10^{-13}	1.2×10^{35}	23.32/17
	(2.2–5.0)	(< 1)			

Power-law model

	Γ	$N_{\rm H}$ (10^{21} H cm^{-2})	$F_{\rm x}$ (erg s^{-1} cm^{-2})	$L_{\rm x}$ (erg s^{-1})	χ^2/d.o.f.
0049−736	5.0	0	6.9×10^{-13}	3.0×10^{35}	6.324/5
	(> 3.6)	(< 11)			
0056−725	1.5	2	3.4×10^{-13}	1.6×10^{35}	5.080/5
	(1.0–2.3)	(< 12)			
DEM S128	2.2	0	3.0×10^{-13}	1.3×10^{35}	18.84/17
	(1.9–2.6)	(< 2)			

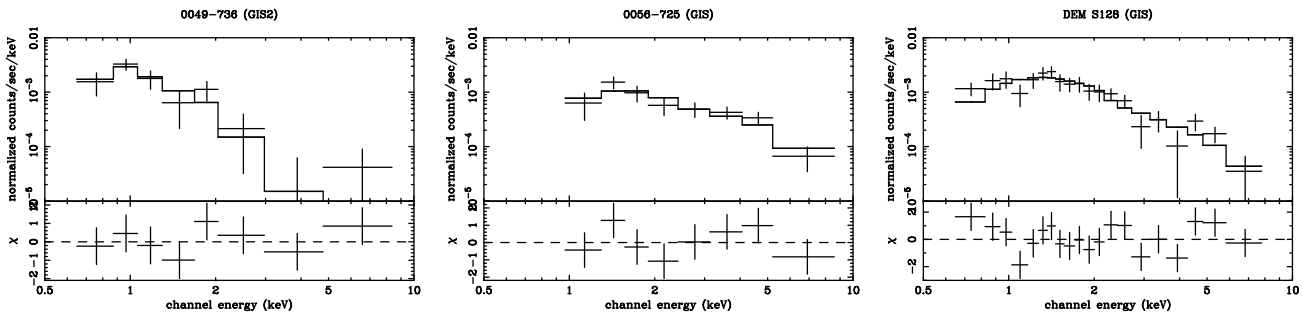

Figure 5.8: GIS spectra of 0049−736, 0056−725 and DEM S128. Crosses represent the observed data, while solid lines represent the the best-fit models (the thermal model for 0049−736 and the power-law model for the others).

5.4 X-ray pulsars

In this section, we present the spectra, folded light curves and other relevant information such as optical counterparts and flux variabilities of the 15 X-ray pulsars in the SMC. Finally we suggest that 13 of the 15 pulsars are X-ray binary pulsars (XBPs).

5.4.1 No. 38: SMC X-1

SMC X-1 is a well known XBP, having a B-type supergiant as a companion (Bildsten et al. 1997). ASCA has observed No. 38 (=SMC X-1) for three times in 1993, 1995 and 1998. The binary system was in a ~ 0.6 day eclipse phase in the second observation. During the first and third observations, random flux variations of a factor ~ 3 were detected.

Coherent pulsations were detected in all the three observations (in the second, only from non-eclipse data). Pulse periods after correction for the Doppler effect (subsection 5.2) were 0.70865(6) s[4], 0.7100(5) s[5] and 0.7065(5) s, respectively. The small interpulse peak in the folded light curves (figure 5.10) reflects a second harmonic in the power spectra.

SMC X-1 has been observed for a long time and its pulse period is monotonically decreasing (e.g. Nagase 1989; Wojdowski et al. 1998; Kahabka & Li 1999). Figure 5.9 shows the pulse period history of SMC X-1. The periods derived from the first and third observations are consistent with the monotonic decrease, while that in the second observation is largely deviated. One possibility is that SMC X-1 experienced a stochastic variation of the spin period as other XBPs (Bildsten et al. 1997).

As noted in subsection 5.3.1, the GIS spectrum in each observation left a soft excess above the power-law model. Adding a blackbody model as a soft component yielded an acceptable fit (table 5.6 and figure 5.10).

[5]Wojdowski et al. (1998) analyzed the same ASCA data. They report that the period was 0.7086390(9) s in 1993 and that they did not detect coherent pulsations in 1995.

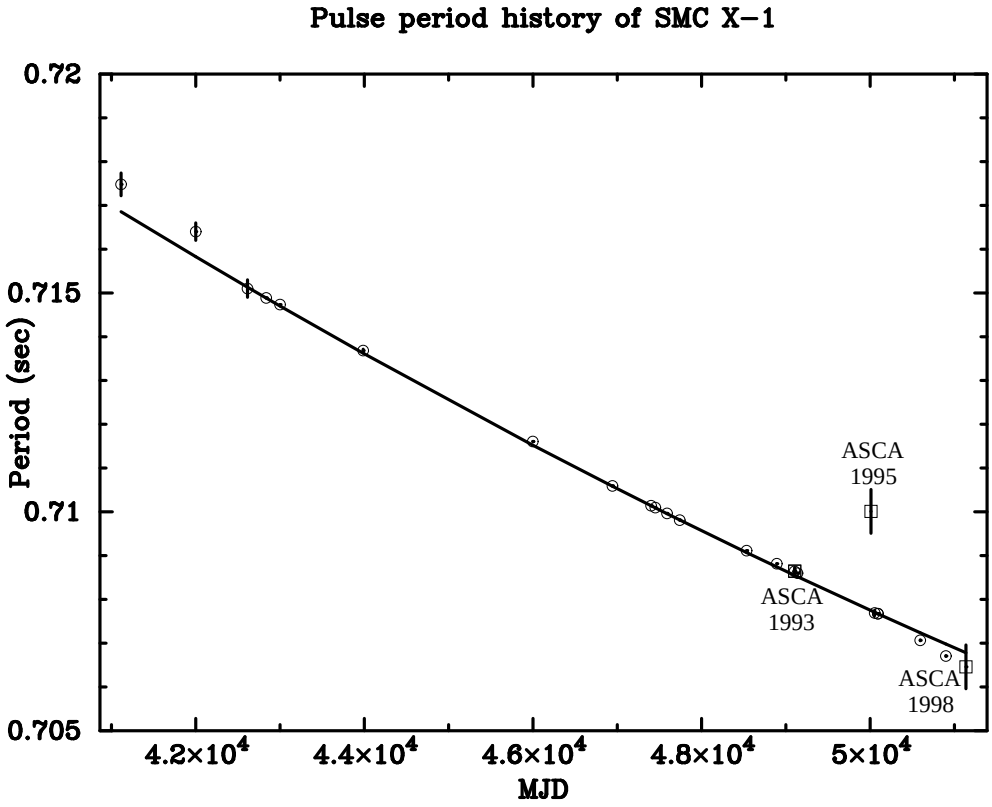

Figure 5.9: The history of pulse period of SMC X-1. Squares and circles represent the periods determined in this work and those taken from Wojdowski et al. (1998) or Kahabka & Li (1999), respectively. The solid line gives the best-fit quadratic function obtained in Wojdowski et al. (1998).

Table 5.6: Best-fit parameters of SMC X-1 with 90% confidence limits. Fluxes and absorption-corrected luminosities are derived from 0.7–10.0 keV band.

Year	Γ	kT (keV)	$N_{\rm H}$ (10^{21} H cm^{-2})	$F_{\rm x}$ (erg s^{-1} cm^{-2})	$L_{\rm x}$ (erg s^{-1})	χ^2/d.o.f.
1993	0.69	0.13	0.4	2.2×10^{-10}	1.1×10^{38}	284.1/210
	(0.61–0.76)	(0.11–0.15)	(0.2–0.6)			
1995*	0.45	0.20	0	8.9×10^{-12}	3.8×10^{36}	163.5/114
	(0.35–0.53)	(0.13–0.29)	(< 2)			
1998	0.35	0.16	2	1.5×10^{-10}	6.7×10^{37}	110.9/77
	(0.27–0.44)	(0.13–0.19)	(< 4)			

*: The spectrum was extracted from non-eclipse data.

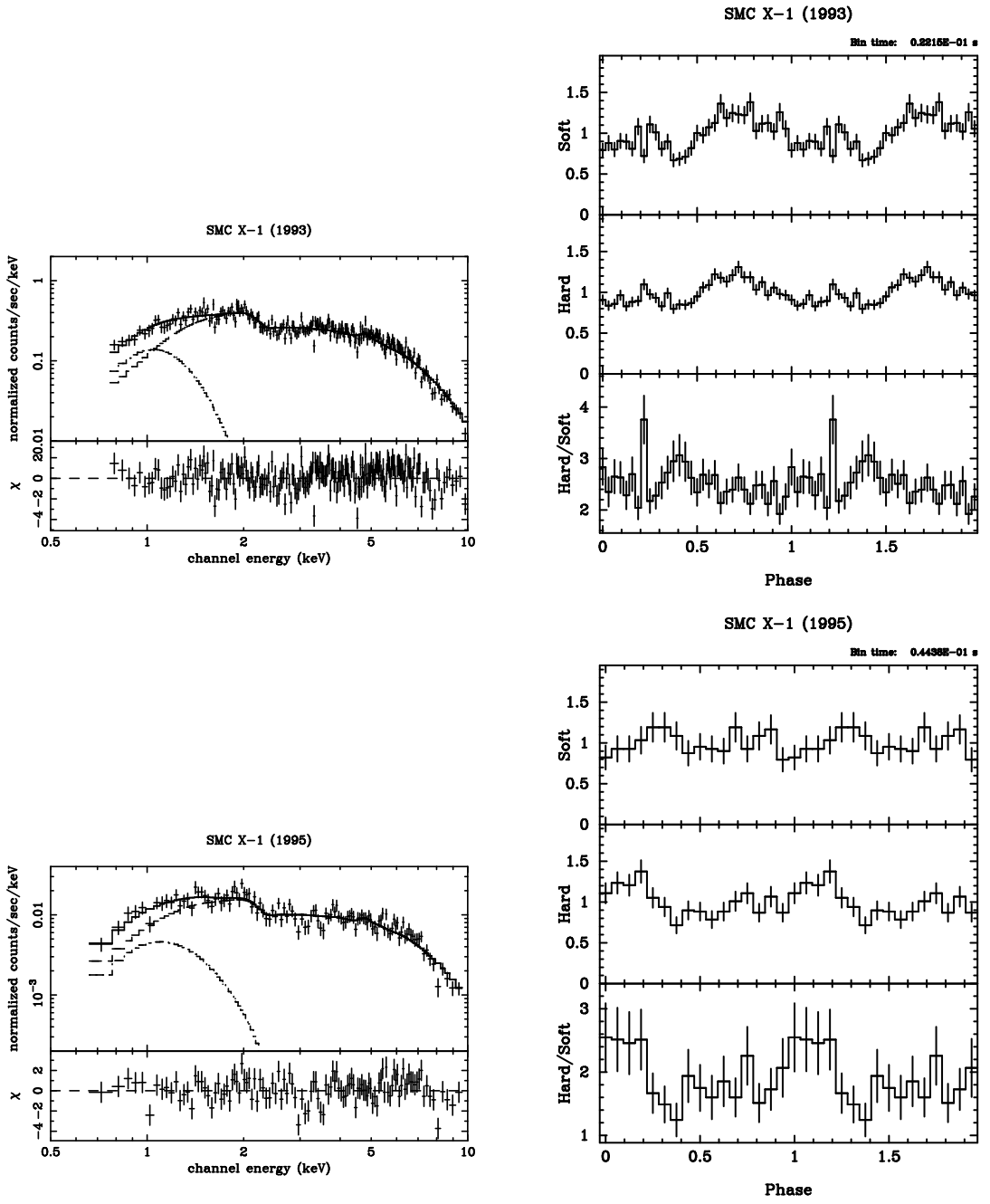

Figure 5.10: Left: The GIS spectra with the best-fit models (see text) of SMC X-1 observed in 1993, 1995 and 1998. Right: The folded light curves in the soft (0.7–2.0 keV; upper panel) and hard (2.0–7.0 keV; middle panel) band. The vertical axes show the normalized count rates. The lower panel shows the intensity ratio of the hard band to the soft band. The spectrum and light curves for the second observation were taken from non-eclipse data.

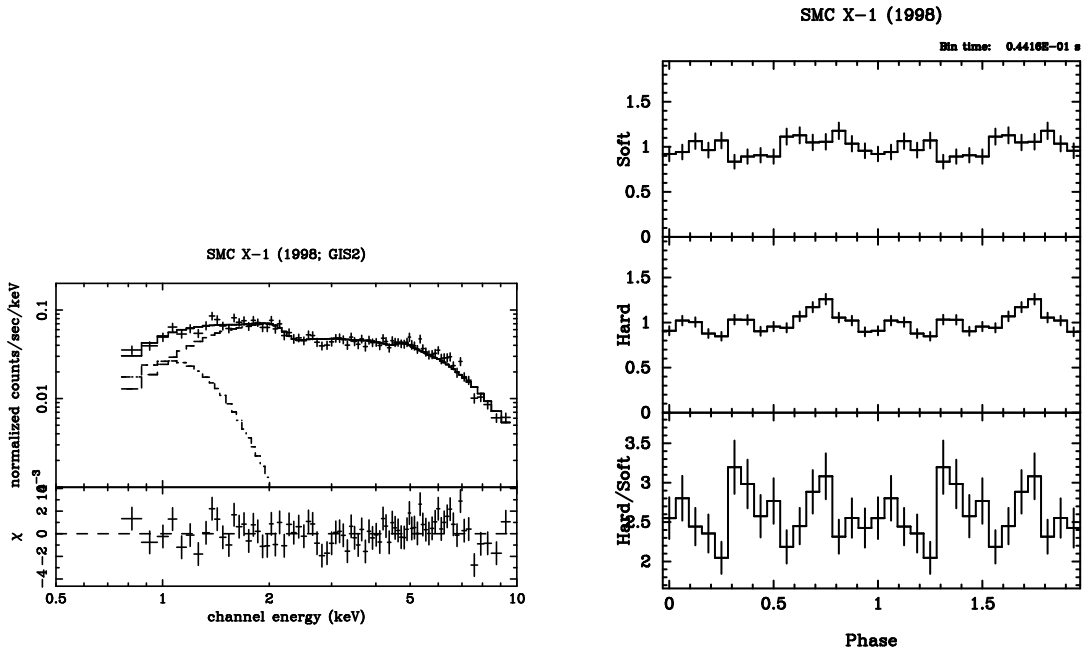

(Figure 5.10 continued.)

5.4.2 No. 25: RX J0059.2−7138

A transient source No. 25=RX J0059.2−7138 was serendipitously detected with ROSAT and ASCA on the same day. Coherent pulsations with 2.7632(2) s period were reported with ROSAT data (Hughes 1994). We detected the same period in the ASCA data, hence the ROSAT result was confirmed. The transient nature indicates that this source is an XBP. Hughes (1994) also identified two stars in the ROSAT error circle, one of which is possibly the optical counterpart.

The GIS spectrum showed a soft excess above an absorbed power-law as noted in Hughes (1994). Adding a blackbody model as a soft component yielded an acceptable fit, although the best-fit parameters are not consistent with those in Hughes (1994).

5.4.3 2E0050.1−7247

Coherent pulsations with 8.8816(2) s period from 2E0050.1−7247 were discovered by Israel et al. (1997). It showed a flux variability of a factor 20. In addition, a Be star was identified in its error circle, hence it is an XBP with a Be star companion. An ASCA observation on Dec. 12, 1998 included the position of 2E0050.1−7247. We did not detect any positive excess above the background level from the position of this source. The upper limit of its flux is estimated to be $\sim 1 \times 10^{-13}$ erg s^{-1} cm^{-2} (0.7–10.0 keV), assuming that the photon index is ~ 1.

Table 5.7: Best-fit parameters of RX J0059.2−7138 with 90% confidence limits. Flux and absorption-corrected luminosity are derived from 0.7–10.0 keV band.

Γ	kT (keV)	$N_{\rm H}$ (10^{21} H cm^{-2})	$F_{\rm x}$ (erg s^{-1} cm^{-2})	$L_{\rm x}$ (erg s^{-1})	χ^2/d.o.f.
0.67	0.13	2	2.5×10^{-10}	1.2×10^{38}	357.1/323
(0.61–0.74)	(0.12–0.15)	(0.6–4)			

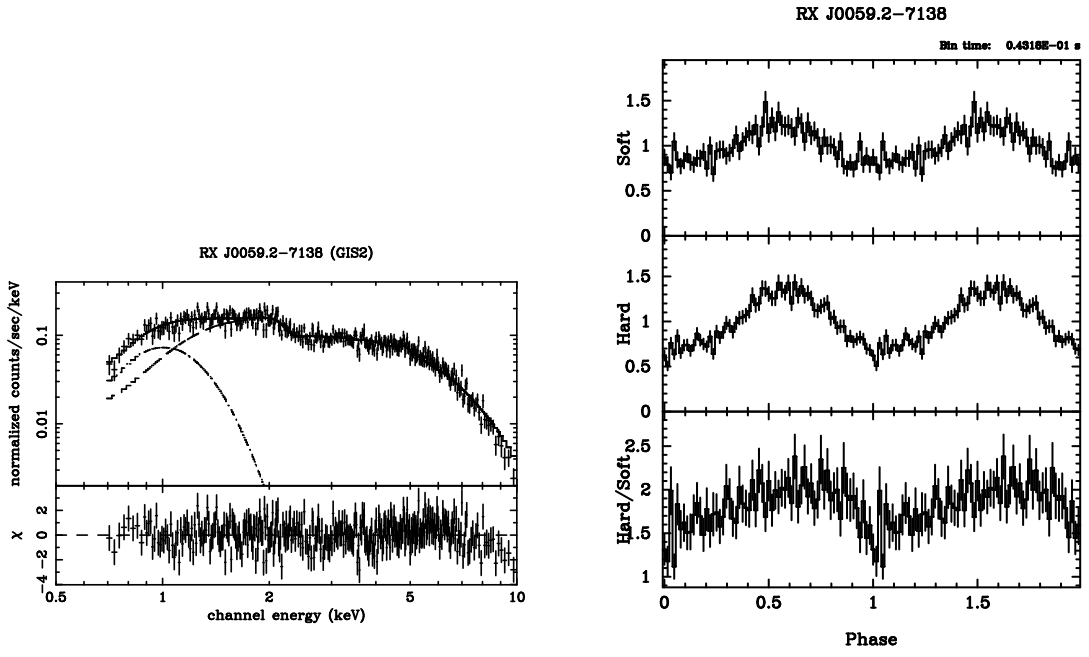

Figure 5.11: The same as figure 5.10, but for RX J0059.2−7138.

5.4.4 No. 11: AX J0051−722

Coherent pulsations with $\sim$ 92 s period were first discovered with an RXTE observation on Nov. 15, 1997 (Marshall et al. 1997). A TOO observation with ASCA on Dec. 12 revealed that No. 11 was pulsating with 91.12(5) s period (Corbet et al. 1997). Since then, this source has been detected in many RXTE/BeppoSAX/ASCA observations, and found to be fading and rebrightening (Lochner et al. 1998; Lochner 1998). Therefore it is certainly an XBP and the orbital period is supposed to be 120 days (Israel et al. 1998).

Energy-resolved pulse profiles are shown in figure 5.12. The deviation from a sinusoid (dip-like structure) is consistent with the strong second and third harmonics in the power spectrum.

Table 5.8: Best-fit parameters of AX J0051−722 with 90% confidence limits. Flux and absorption-corrected luminosity are derived from 0.7–10.0 keV band.

Γ	$N_{\rm H}$ (10^{21} H cm^{-2})	$F_{\rm x}$ (erg s^{-1} cm^{-2})	$L_{\rm x}$ (erg s^{-1})	χ^2/d.o.f.
1.0	10	9.5×10^{-12}	4.8×10^{36}	31.30/20
(0.7–1.3)	(5–16)			

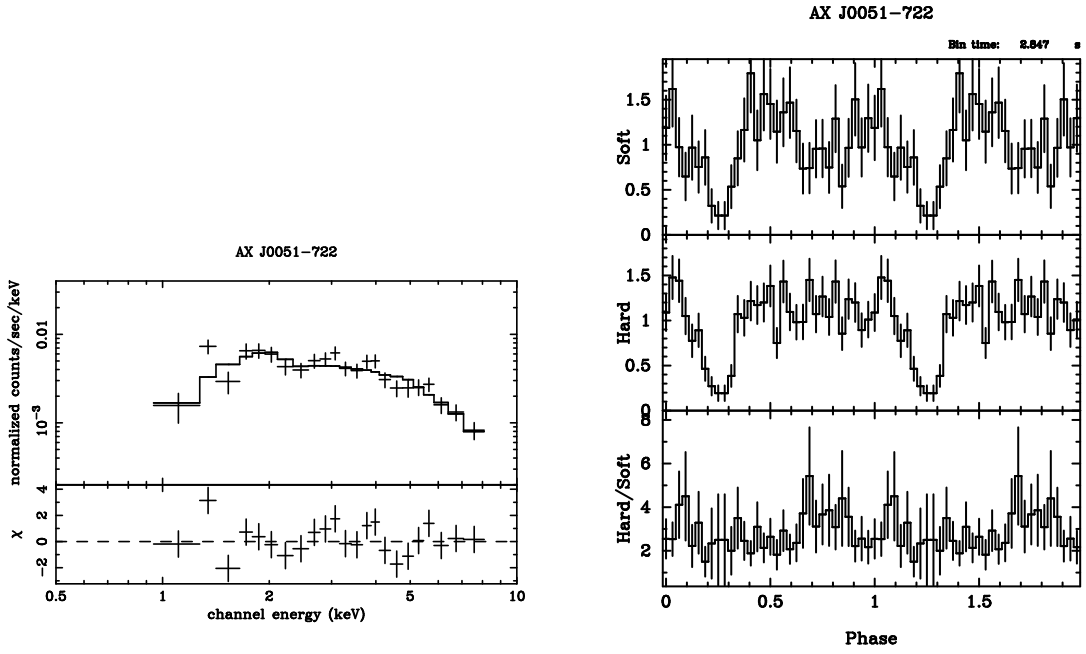

Figure 5.12: The same as figure 5.10, but for AX J0051−722.

In K99, RX J0051.3−7216 is identified as a ROSAT counterpart of AX J0051−722. However, we note the possibility of misidentification because the separation between the ROSAT position and ASCA position is $\gtrsim 2'$, which is significantly larger than the positional uncertainty of ROSAT/ASCA.

5.4.5 No. 15: 1WGA J0053.8−7226

The ASCA observation on Dec. 12, 1998 also revealed that No. 15 was pulsating with a period of 46.63(4) s (Corbet et al. 1997). A ROSAT variable source 1WGA J0053.8−7226 and a Be star exist in its error circle (Buckley et al. 1997). These facts indicate that this is an XBP with a Be star companion.

Table 5.9: Best-fit parameters of 1WGA J0053.8−7226 with 90% confidence limits. Flux and absorption-corrected luminosity are derived from 0.7–10.0 keV band.

Γ	$N_{\rm H}$ (10^{21} H cm^{-2})	$F_{\rm x}$ (erg s^{-1} cm^{-2})	$L_{\rm x}$ (erg s^{-1})	χ^2/d.o.f.
0.8 (0.7–0.9)	1 (< 2)	1.2×10^{-11}	5.2×10^{36}	57.11/57

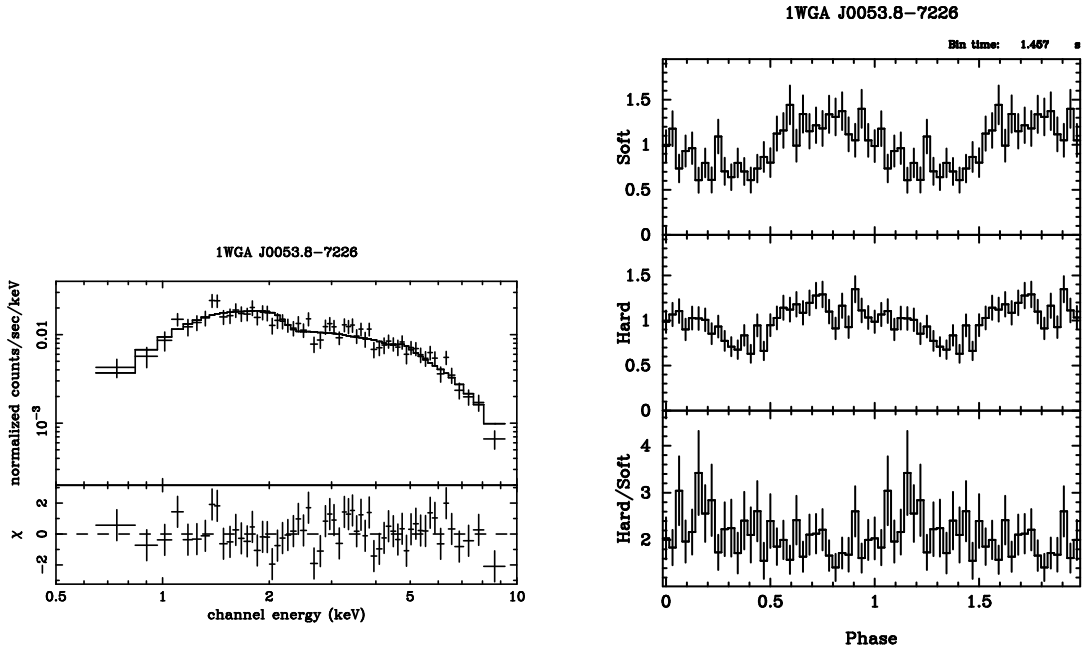

Figure 5.13: The same as figure 5.10, but for 1WGA J0053.8−7226.

5.4.6 XTE J0054−720

XTE J0054−720 was found to exhibit coherent pulsations with RXTE. Its pulse period and flux in 2–10 keV band were 169.30 s and $\sim 6.0 \times 10^{-11}$ erg s^{-1} cm^{-2} on Dec. 17, 1997, and 168.40 s and $\sim 3.3 \times 10^{-11}$ erg s^{-1} cm^{-2} on Dec. 20, 1997, respectively (Lochner et al. 1998). The transient and fading behaviour indicates that XTE J0054−720 is an XBP.

A part of its error circle ($\sim 10'$ radius) is involved in the ASCA observations. The only one source No. 17 was detected in the error circle during the ASCA observation on Dec. 14, 1997, although coherent pulsations were not detected. The flux of No. 17 ($\sim 3.6 \times 10^{-13}$ erg s^{-1} cm^{-2}; 2–10 keV) is about 100 times smaller than that reported with RXTE. The ROSAT counterpart of No. 17, RX J0055.4−7210, is regarded as a background source in Filipovic et al. (1998).

We note that a ROSAT source RX J0052.9−7158 is also in the error circle of XTE J0054−720 (and out of our observation fields). It was reported to have a large flux variability and a Be star companion (Cowley et al. 1997), hence may be a counterpart of XTE J0054−720.

5.4.7 No. 16: XTE J0055−724

An RXTE observation on Jan. 22, 1998 and a BeppoSAX observation on Jan. 28 revealed that XTE J0055−724=1SAX J0054.9−7226 was exhibiting coherent pulsations with 58.969(1) s period (Marshall & Lochner 1998; Santangelo et al. 1998). An ASCA source No. 16 was detected in the observation on Nov. 14, 1997. We performed the epoch folding search, then found a peak at 59.00(2) s. Therefore No. 16 is the counterpart of XTE J0055−724.

This source has been involved in various observation fields of some satellites. Changes of its flux and pulse period are reported as in table 5.10. In addition, two stars with an H_α emission line were detected in the error circle (Israel et al. 1998). The flux variability and existence of the optical counterparts indicate that XTE J0055−724 is an XBP with a Be star companion.

5.4.8 No. 3: AX J0049−729

Coherent pulsations with 74.8(4) s period were first reported with RXTE (Corbet et al. 1997) in the direction of SMC X-3. However, the positional uncertainty was very large ($\sim 2^\circ$). During this analysis, we found that No. 3 was pulsating with 74.68(3) s period and determined its position more accurately (Yokogawa & Koyama 1998a).

In the error circle of AX J0049−729, there exists a ROSAT source RX J0049.1−7250, which was reported to show a flux variability by a factor of 12 (Kahabka & Pietsch 1996). The ASCA

Table 5.10: Changes of flux and pulse period of XTE J0055−724.

Observed Date	Satellite	Flux in 2–10 keV (erg s^{-1} cm^{-2})	Period (sec.)	Ref.
1991 Oct.	ROSAT	Not reported	59.072(1)	[1]
1997 Nov. 14	ASCA	2.5×10^{-12}	59.00(2)	This work
1997 Dec. 12	ASCA	No detection	—	This work
1998 Jan. 12	RXTE	No detection	—	[2]
1998 Jan. 22	RXTE	6×10^{-11}	59.0(2)	[2]
1998 Jan. 28	BeppoSAX	1.9×10^{-11}	58.969(1)	[1]
1998 Jul. 24	BeppoSAX	7×10^{-12}	58.95(1)	[3]

References: [1]Santangelo et al. 1998, [2]Marshall & Lochner 1998, [3]Israel et al. 1998.

Table 5.11: Best-fit parameters of XTE J0055−724 with 90% confidence limits. Flux and absorption-corrected luminosity are derived from 0.7–10.0 keV band.

Γ	$N_{\rm H}$ (10^{21} H cm^{-2})	$F_{\rm x}$ (erg s^{-1} cm^{-2})	$L_{\rm x}$ (erg s^{-1})	χ^2/d.o.f.
0.4 (0.1–1.0)	0.02 (< 10)	2.7×10^{-12}	1.2×10^{36}	9.258/15

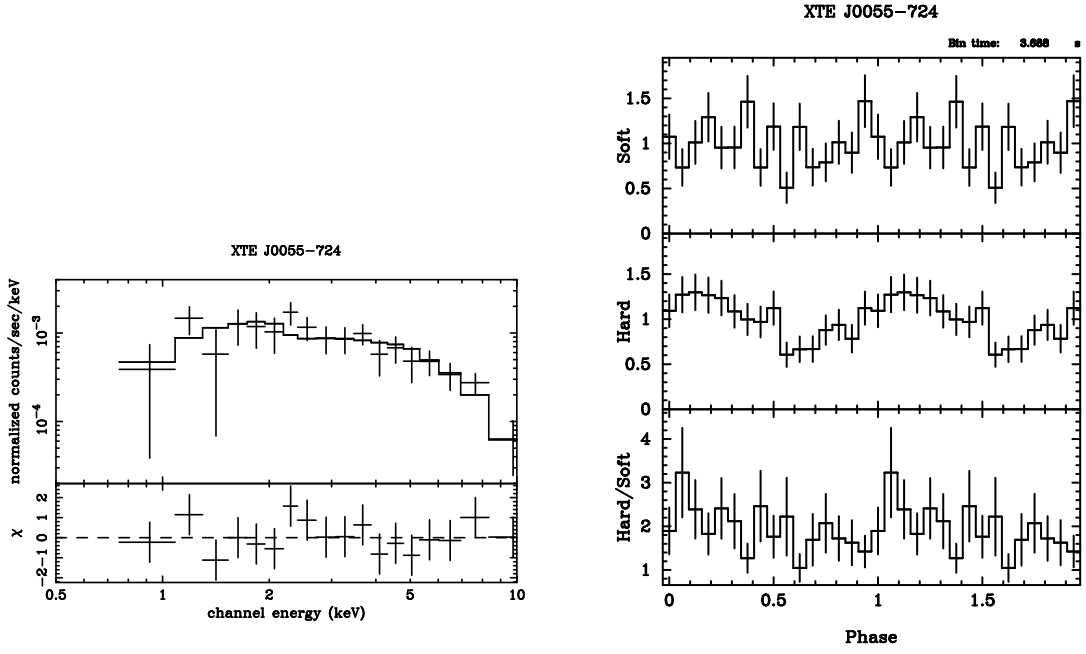

Figure 5.14: The same as figure 5.10, but for XTE J0055−724.

flux ($\sim 1.5 \times 10^{-11}$ erg s^{-1} cm^{-2}; 0.3–2.4 keV) is comparable of the ROSAT flux in the higher state. This large flux variability indicates that AX J0049−729 is an XBP.

Table 5.12: Best-fit parameters of AX J0049−729 with 90% confidence limits. Flux and absorption-corrected luminosity are derived from 0.7–10.0 keV band.

Γ	$N_{\rm H}$ (10^{21} H cm^{-2})	$F_{\rm x}$ (erg s^{-1} cm^{-2})	$L_{\rm x}$ (erg s^{-1})	χ^2/d.o.f.
1.0 (0.9–1.2)	4 (2–7)	1.1×10^{-11}	5.5×10^{36}	45.82/59

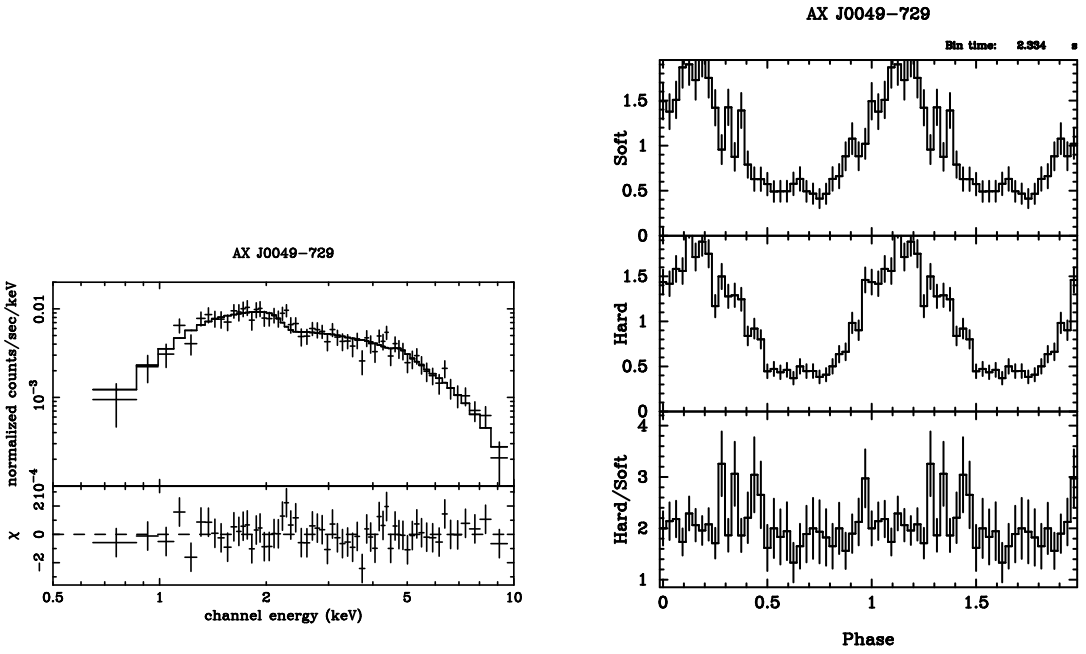

Figure 5.15: The same as figure 5.10, but for AX J0049−729.

5.4.9 No. 8: AX J0051−733

Coherent pulsations with 323.2(5) s period from No. 8 (AX J0051−733) were first detected during this analysis (Yokogawa & Koyama 1998b).

A ROSAT source RX J0050.7−7316 (K99) is in the error circle of AX J0051−733, while there is no Einstein counterpart (WW92). The ASCA flux ($\sim 8 \times 10^{-13}$ erg s^{-1} cm^{-2}; 0.3–3.5 keV) is at least 10 times larger than the detection limit of WW92. In addition, a variable

Be star with a modulation of 0.708 days period was detected in the error circle (Cowley et al. 1997; Cook 1998; Schmidtke & Cowley 1998). Therefore AX J0051−733 is certainly an XBP with a Be star companion.

Table 5.13: Best-fit parameters of AX J0051−733 with 90% confidence limits. Flux and absorption-corrected luminosity are derived from 0.7–10.0 keV band.

Γ	$N_{\rm H}$ (10^{21} H cm^{-2})	$F_{\rm x}$ (erg s^{-1} cm^{-2})	$L_{\rm x}$ (erg s^{-1})	χ^2/d.o.f.
0.6	0	3.6×10^{-12}	1.5×10^{36}	29.46/25
(0.4–0.9)	(< 4)			

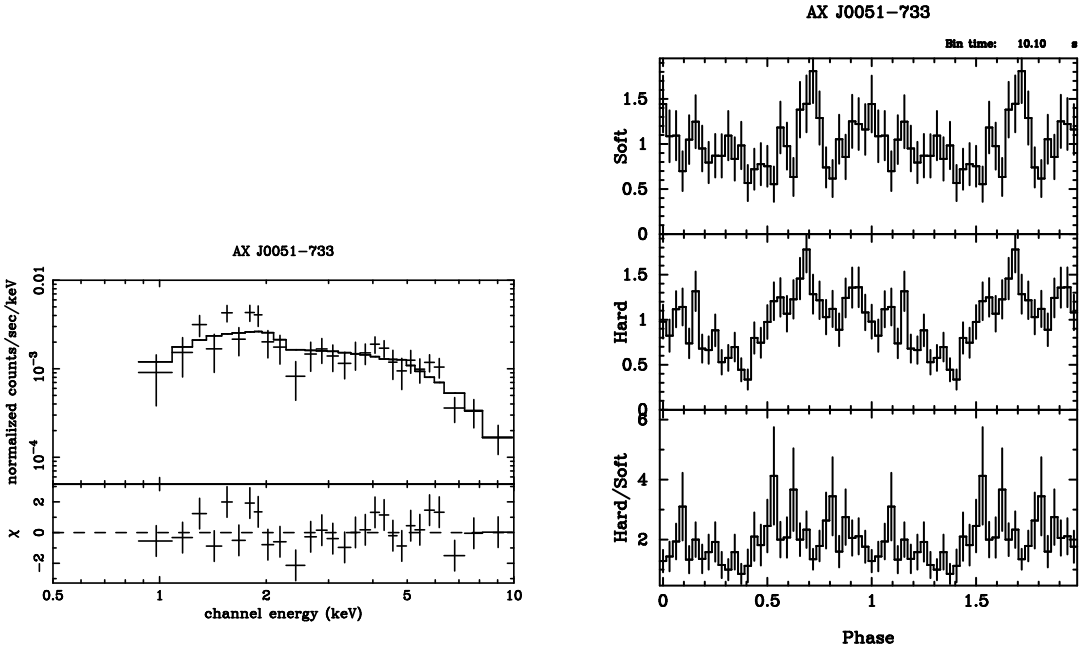

Figure 5.16: The same as figure 5.10, but for AX J0051−733.

5.4.10 No. 20: AX J0058−720

Coherent pulsations with 280.4(4) s period from No. 20 (AX J0058−720) were first detected during this analysis (Yokogawa & Koyama 1998b). In the error circle of AX J0058−720, there exist an Einstein source SMC41 in WW92 and a ROSAT source RX J0057.8−7202 in K99 (although it is not identified as the counterpart in K99). The ASCA flux corresponds to

$\sim 6 \times 10^{-13}$ erg s^{-1} cm^{-2} (0.3–3.5 keV) and $\sim 3 \times 10^{-13}$ erg s^{-1} cm^{-2} (0.3–2.4 keV). These are about 10/5 times larger than the Einstein/ROSAT flux. The variability indicates that AX J0058−720 is an XBP.

Table 5.14: Best-fit parameters of AX J0058−720 with 90% confidence limits. Flux and absorption-corrected luminosity are derived from 0.7–10.0 keV band.

Γ	$N_{\rm H}$ (10^{21} H cm^{-2})	$F_{\rm x}$ (erg s^{-1} cm^{-2})	$L_{\rm x}$ (erg s^{-1})	χ^2/d.o.f.
1.0 (0.7–1.3)	4 (0.2–9)	2.4×10^{-12}	1.1×10^{36}	45.14/34

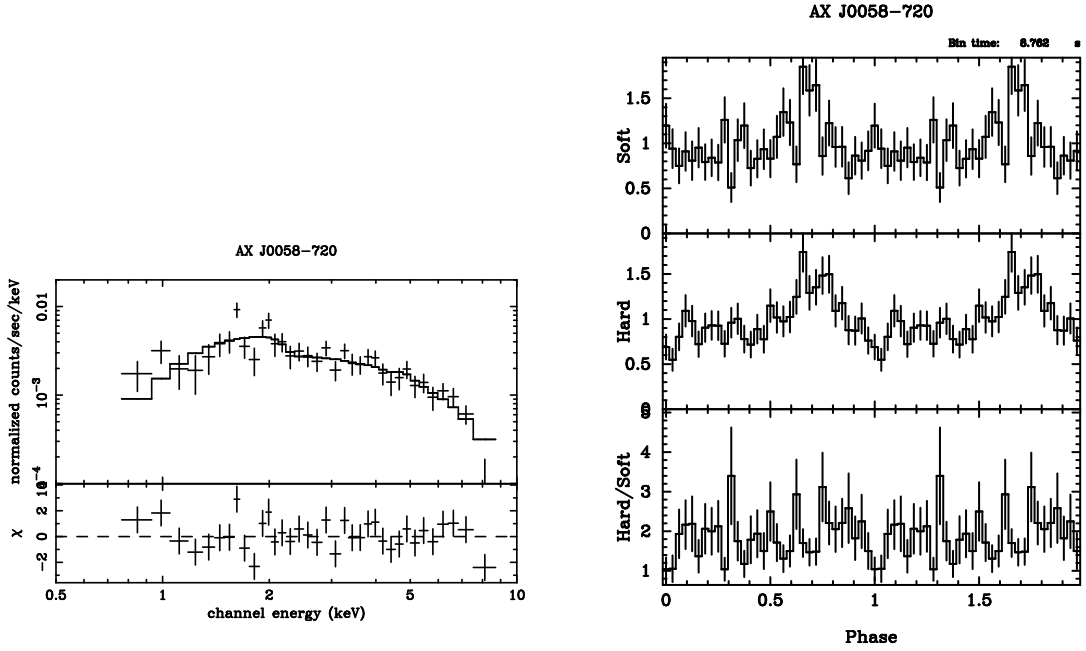

Figure 5.17: The same as figure 5.10, but for AX J0058−720.

5.4.11 No. 29: 1SAX J0103.2−7209

RX J0103.2−7209, a ROSAT counterpart of 1SAX J0103.2−7209, was spatially resolved with ROSAT HRI (Hughes & Smith 1994; Ye et al. 1995). It is a point source lying in a shell-like radio SNR 0101−724. X-rays from the radio shell were not detected. In addition, a Be star was discovered in the error circle. Therefore RX J0103.2−7209 is certainly a Be/X binary system.

Table 5.15: Best-fit parameters of 1SAX J0103.2−7209 with 90% confidence limits. Fluxes and absorption-corrected luminosities are derived from 0.7–10.0 keV band.

Year	Γ	$N_{\rm H}$ (10^{21} H cm^{-2})	$F_{\rm x}$ (erg s^{-1} cm^{-2})	$L_{\rm x}$ (erg s^{-1})	χ^2/d.o.f.
1993	1.0	6	1.3×10^{-12}	6.3×10^{35}	8.438/13
	(0.4–1.8)	(< 19)			
1996	0.8	0	1.1×10^{-12}	4.9×10^{35}	11.60/20
	(0.6–1.0)	(< 3)			
1997	0.1	0	1.1×10^{-12}	4.9×10^{35}	15.31/9
	(−0.8–1.0)	(< 25)			
Sum	0.7	0	1.1×10^{-12}	4.7×10^{35}	19.30/24
	(0.6–1.0)	(< 4)			

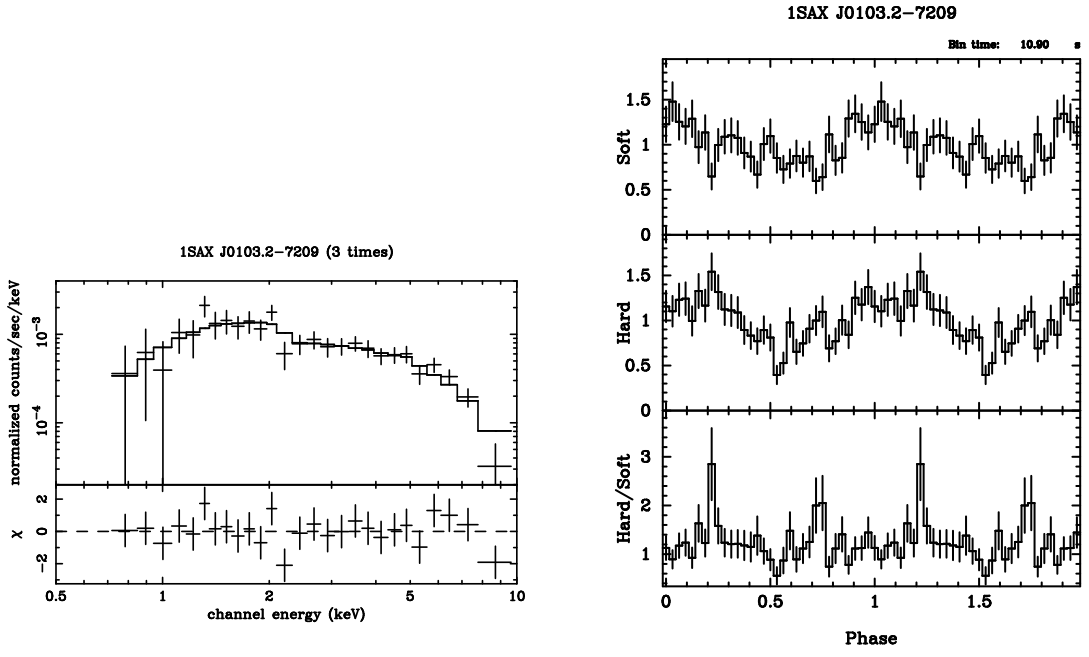

Figure 5.18: The same as figure 5.10, but for 1SAX J0103.2−7209. The spectrum is the summed one, while the light curves were derived from the data obtained in 1996.

Coherent pulsations with 345.2(1) s period from 1SAX J0103.2−7209 were first discovered in a BeppoSAX observation on July 27, 1998 (Israel et al. 1998). Therefore it is an XBP with a Be star companion. Its ASCA counterpart No. 29 (AX J0103−722) has been observed for three times, on May 12, 1993, May 21, 1996, and Nov. 14, 1997. We detected coherent pulsations with 348.9(3) s period from the data obtained in 1996, which had the highest statistics (Yokogawa & Koyama 1998d). We could not detect coherent pulsations from the data obtained in the other observations, probably due to the limited statistics.

Derived spectral parameters in the three observations were consistent with each other. Therefore we combined the three spectra into one and fit it again ("Sum" in table 5.15).

The ASCA flux was derived to be $\sim 1.0 \times 10^{-12}$ erg s^{-1} cm^{-2} (2–10 keV) in each observation. This value is 3 times smaller than the SAX flux ($\sim 3 \times 10^{-12}$ erg s^{-1} cm^{-2}; 2–10 keV). The variability confirms its binary nature.

5.4.12 No. 32: AX J0105−722

Coherent pulsations of 3.34300(3) s period were first detected from No. 32 (AX J0105−722) during this analysis (Yokogawa & Koyama 1998c) as described in section 5.2. The significance of pulse detection was 99.5%.

The error circle of AX J0105−722 includes a ROSAT source RX J0105.3−7210 and an Einstein source SMC53, both of which were identified with a radio SNR DEM S128 (Filipovic et al. 1998; WW92). The ASCA flux is $\sim 2.9 \times 10^{-13}$ erg s^{-1} cm^{-2} (0.3–2.4 keV) or $\sim 3.3 \times 10^{-13}$ erg s^{-1} cm^{-2} (0.3–3.5 keV). These are comparable with fluxes of ROSAT or Einstein (the discrepancy is within a factor ~ 2).

There are some possible candidates of the nature of AX J0105−722. Its photon index (~ 2.2), relatively low luminosity (10^{35} erg s^{-1}; 0.7–10.0 keV) and the association with an SNR are common with SNRs emitting synchrotron X-rays (e.g. SN1006, Koyama et al. 1995; RX J1713.7−3946, Koyama et al. 1997), Crab-like SNRs or Soft γ-ray repeaters (SGR1806−20, Kouveliotou et al. 1998; SGR1900+14, Kouveliotou et al. 1999; Murakami et al. 1999; Hurley et al. 1999). Whether AX J0105−722 is pulsating or not and, if it is pulsating, the pulse period and the period derivative carry the essential information to distinguish between these possible candidate classes. Further observations with better photon statistics are needed.

Table 5.16: Best-fit parameters of AX J0105−722 with 90% confidence limits. Flux and absorption-corrected luminosity are derived from 0.7–10.0 keV band.

Γ	$N_{\rm H}$ (10^{21} H cm^{-2})	$F_{\rm x}$ (erg s^{-1} cm^{-2})	$L_{\rm x}$ (erg s^{-1})	χ^2/d.o.f.
2.2	0	3.0×10^{-13}	1.3×10^{35}	18.84/17
(1.9–2.6)	(< 2)			

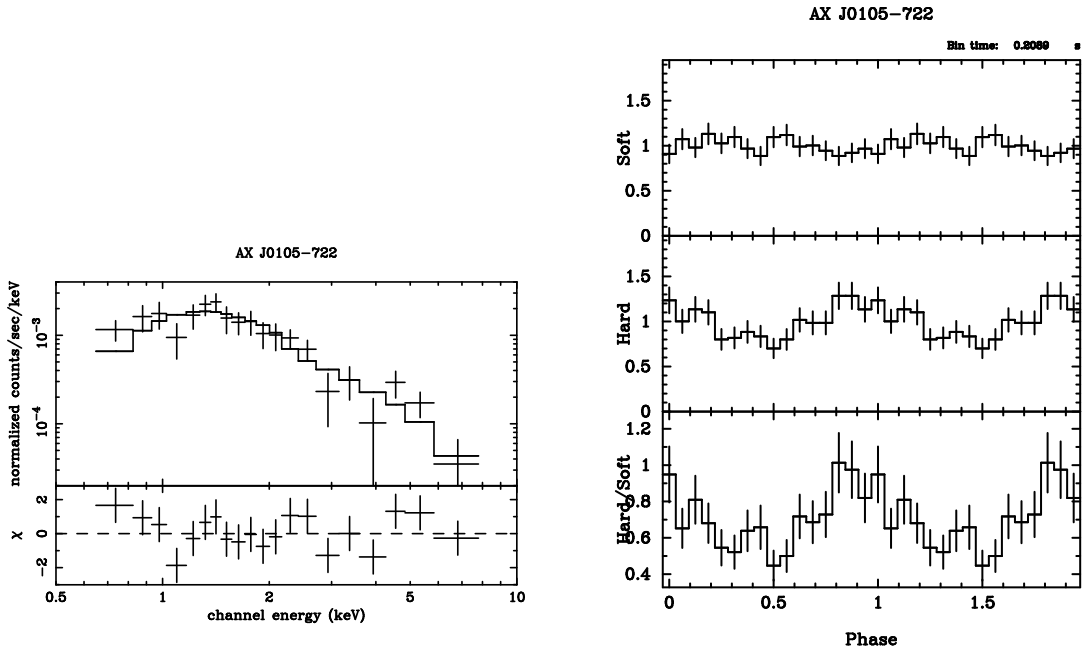

Figure 5.19: The same as figure 5.10, but for AX J0105−722.

5.4.13 No. 5: AX J0049−732

Coherent pulsations with 9.1321(4) s period from No. 5 (AX J0049−732) were first detected during this analysis (Imanishi, Yokogawa & Koyama 1998) as described in section 5.2.

ROSAT sources 1WGA J0049.4−7310 and 1WGA J0049.1−7311 are in the error circle of AX J0049−732. We took their ROSAT spectra from HEASARC archive system and fitted each of them with an absorbed power-law model. The sum of their fluxes was derived to be $\sim 4 \times 10^{-14}$ erg s^{-1} cm^{-2} (0.3–2 keV). As noted in subsection 5.3.1, ASCA spectrum of AX J0049−732 was heavily contaminated by that of the SNR 0047−735 (separated by only $\sim 2'$), therefore an accurate estimation of its flux was difficult. Some more observations with a better spatial resolution and photon statistics are needed to reveal the nature of AX J0049−732.

5.4.14 No. 37: XTE J0111.2−7317

XTE J0111.2−7317 was serendipitously discovered with RXTE and CGRO, and coherent pulsations with ~ 31 s period were detected (Chakrabarty et al. 1998a; Wilson et al. 1998). A TOO observation was carried out by ASCA on Nov. 19, 1998, then No. 37 was detected (Chakrabarty et al. 1998b). Coherent pulsations with 30.9497(6) s period were detected, hence No. 37 is certainly the counterpart of XTE J0111.2−7317. The transient behaviour and the existence of a Be star in the error circle (Israel et al. 1999) indicate that XTE J0111.2−7317 is an XBP.

As noted in subsection 5.3.1, the GIS spectrum left a soft excess above an absorbed power-law model. Adding a blackbody model as a soft component yielded an acceptable fit (figure 5.20 and table 5.17).

5.4.15 No. 14: RX J0052.1−7319

Coherent pulsations with 15.3 s period from a variable X-ray source RX J0052.1−7319 were discovered in ROSAT and CGRO observations on 1996 (Lamb et al. 1999; Kahabka 1999). In addition, a Be star was discovered in the error circle (Israel et al. 1999), hence RX J0052.1−7319 is certainly an XBP.

The position of No. 14 coincides with that of RX J0052.1−7319. However, we detected no sign of coherent pulsations by either the FFT analysis or the epoch folding search. Therefore it is not clear whether No. 14 is really the counterpart of RX J0052.1−7319.

Table 5.17: Best-fit parameters of XTE J0111.2−7317 with 90% confidence limits. Flux and absorption-corrected luminosity are derived from 0.7–10.0 keV band.

Γ	kT (keV)	$N_{\rm H}$ (10^{21} H cm^{-2})	$F_{\rm x}$ (erg s^{-1} cm^{-2})	$L_{\rm x}$ (erg s^{-1})	χ^2/d.o.f.
0.79	0.144	2.3	3.7×10^{-10}	1.7×10^{38}	452.9/445
(0.76–0.82)	(0.137–0.150)	(1.6–3.0)			

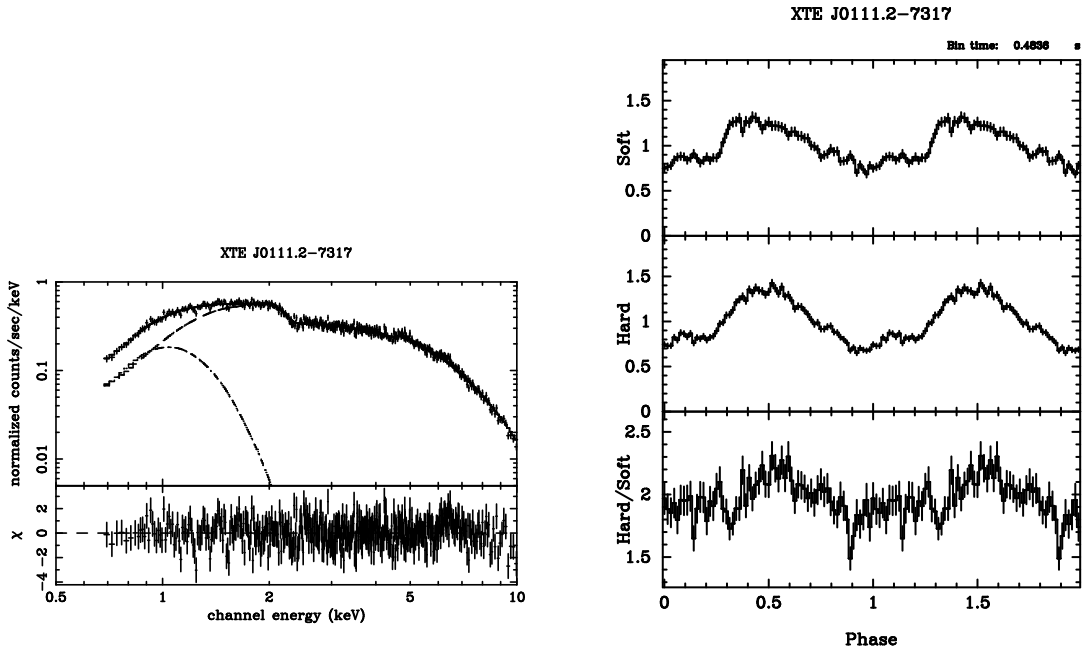

Figure 5.20: The same as figure 5.10, but for XTE J0111.2−7317.

5.5 The 1st ASCA catalogue of X-ray sources in the SMC

Column 1 Source number. Source extraction is described in subsection 5.1.1.

Columns 2–3 Equatorial coordinates (J2000). Radius of the error circle is $\sim 1'$ for on-axis sources and $\sim 2'$ for sources detected on the very edge of GIS.

Column 4 HR (hardness ratio) defined in subsection 5.1.2.

Columns 5–6 Best-fit parameters derived from the spectral fitting described in section 5.3. Thermal models were applied to No. 1, No. 12, No. 24, No. 30 and No. 31 (subsection 5.3.2). Photon index Γ, temperature kT (keV; marked with *) and column density $N_{\rm H}$ (10^{21} H cm^{-2}) are presented. Note that the two-component model (power-law and blackbody) was applied for RX J0059.2−7138 (No. 25), XTE J0111.2−7317 (No. 37) and SMC X-1 (No. 38). See subsection 5.3.1.

Column 7 X-ray flux in 0.7–10.0 keV (10^{-12} erg cm^{-2} s^{-1}) for the best-fit model.

Column 8 Observed luminosity in 0.7–10.0 keV (10^{36} erg s^{-1}).
$L_{\rm obs} \equiv F_{\rm x} \times 4\pi d^2$, where d is assumed to be 60 kpc.

Column 9 X-ray luminosity in 0.7–10.0 keV (10^{36} erg s^{-1}) after correction for the absorption.

Column 10 Source class.
TS : Thermal SNR (subsection 5.3.2).
RS : Radio SNR which is not classified as a thermal SNR.
TSc: Thermal SNR candidate (subsection 6.1.4).
BP : XBP (section 5.4).
P : Pulsar which is not classified as an XBP.
BPc: XBP candidate (subsection 6.1.4).
NH :Non-pulsating HMXB (table 6.2).
UN :Unclassified source.

Column 11 Names of the source. "Wn" or "Kn" represent the source No. n in the catalogues of WW92 or K99.
*: Not regarded as the counterpart in K99.
†: Regarded as the counterpart in K99, but the separation is $\gtrsim 2'$.

Column 12 Comments. Pulse periods and optical counterparts for X-ray pulsars and HMXBs are also given (see table 5.1 and 6.2 for references).

Table 5.18: The 1st ASCA catalogue of X-ray sources in the SMC.

No.	R.A.	Dec.	HR	Γ, $kT^{\star}$	$N_{\rm H}$	$F_{\rm x}$	$L_{\rm obs}$	$L_{\rm x}$	Class
1	00:47:30	−73:09:13	−0.67	0.7 (0.6–0.8)*	4 (3–6)	0.35	0.15	0.39	TS
2	00:47:30	−73:12:33	0.22	1.0 (0.8–1.2)	0 (< 2)	0.69	0.30	0.30	BPc
3	00:49:00	−72:51:40	0.39	1.0 (0.9–1.2)	4 (2–7)	11	4.7	5.5	BP
4	00:49:12	−73:14:06	—	—	—	—	—	—	RS
5	00:49:24	−73:12:21	—	—	—	—	—	—	P
6	00:49:34	−73:30:45	0.23	1.7 (0.6–3.7)	6 (< 40)	0.57	0.25	0.32	BPc
7	00:49:38	−73:23:48	0.50	1.5 (0.3–3.8)	16 (< 69)	0.91	0.39	0.55	BPc
8	00:50:47	−73:15:51	0.34	0.6 (0.4–0.9)	0 (< 4)	3.6	1.5	1.5	BP
9	00:50:50	−72:42:19	−0.16	2.2 (1.5–3.6)	2 (< 11)	0.39	0.17	0.20	UN
10	00:51:05	−72:27:59	0.58	0.1 (−1.0–1.3)	0 (< 21)	0.58	0.25	0.25	BPc
11	00:51:11	−72:14:01	0.55	1.0 (0.7–1.3)	10 (5–16)	9.5	4.1	4.8	BP
12	00:51:12	−73:20:06	−0.68	0.7 (0.3–1.0)*	0.02 (< 5)	0.64	0.28	0.28	TSc
13	00:51:55	−73:10:19	0.17	1.0 (0.04–2.4)	0 (< 18)	0.86	0.37	0.37	NH
14	00:52:20	−73:19:00	0.83	3.3 (> 0.4)	58 (< 300)	0.68	0.29	2.5	BP
15	00:53:56	−72:26:54	0.37	0.8 (0.7–0.9)	1 (< 2)	12	5.2	5.2	BP
16	00:55:00	−72:25:38	0.51	0.4 (0.1–1.0)	0.02 (< 10)	2.7	1.2	1.2	BP
17	00:55:38	−72:11:03	0.01	1.4 (0.8–2.3)	0 (< 5)	0.46	0.20	0.20	UN
18	00:57:25	−72:25:14	−0.06	5.3 (> 2.1)	35 (5–108)	0.13	0.056	2.6	UN
19	00:57:39	−72:19:24	0.15	1.6 (0.9–2.6)	4 (< 15)	0.42	0.18	0.21	UN
20	00:57:58	−72:02:56	0.37	1.0 (0.7–1.3)	4 (0.2–9)	2.4	1.0	1.1	BP
21	00:58:20	−72:17:56	0.20	1.5 (1.0–2.3)	2 (< 12)	0.34	0.15	0.16	RS,BPc
22	00:58:22	−72:30:36	1.00	2.6 (0.2–6.0)	89 (29–230)	0.70	0.30	1.4	NH
23	00:59:29	−72:22:44	0.25	1.0 (0.7–1.5)	0 (< 5)	0.75	0.32	0.32	BPc
24	00:59:30	−72:10:16	−0.68	0.7 (0.6–0.8)*	4 (2–5)	0.35	0.15	0.39	TS
25	00:59:32	−71:38:20	0.34	0.67 (0.61–0.74) 0.13 (0.12–0.15)*	2 (0.6–4)	250	110	120	BP
26	01:00:44	−72:11:30	−0.37	3.2 (2.4–4.7)	3 (< 11)	0.36	0.15	0.23	UN
27	01:01:24	−72:11:08	0.43	0.6 (0.4–0.9)	1 (< 5)	1.7	0.73	0.73	BPc
28	01:01:51	−72:23:15	0.20	1.4 (0.8–2.2)	5 (< 14)	0.51	0.22	0.26	BPc
29	01:03:15	−72:09:01	0.36	0.7 (0.6–1.0)	0 (< 4)	1.1	0.47	0.47	BP,RS
30	01:03:58	−72:01:50	−0.88	— See subsection 5.3.2. —		14	6.0	7.2	TS
31	01:05:02	−72:22:58	−0.88	0.37 (0.32–0.38)*	0 (< 1)	1.1	0.47	0.47	TS
32	01:05:06	−72:11:08	−0.20	2.2 (1.9–2.6)	0 (< 2)	0.30	0.13	0.13	RS,P
33	01:05:27	−72:13:40	−0.28	2.6 (2.1–3.5)	0 (< 3)	0.16	0.069	0.069	UN
34	01:05:46	−72:03:38	—	—	—	—	—	—	—
35	01:06:42	−72:24:36	0.16	1.3 (0.9–2.0)	0.3 (< 8)	0.38	0.16	0.16	UN
36	01:07:13	−72:34:41	0.68	4.2 (1.5–9.7)	51 (12–150)	0.19	0.082	1.8	UN
37	01:11:15	−73:16:50	0.33	0.79 (0.76–0.82) 0.144 (0.137–0.150)*	2.3 (1.6–3.0)	370	160	170	BP
38	01:16:58	−73:26:38	0.43	0.69 (0.61–0.76) 0.13 (0.11–0.15)*	4 (2–6)	220	95	110	BP
	01:17:11	−73:26:37	0.40	0.45 (0.35–0.53) 0.20 (0.13–0.29)*	0 (< 2)	8.9	3.8	3.8	BP
	01:17:12	−73:26:25	0.44	0.35 (0.27–0.44) 0.16 (0.13–0.19)*	2 (< 4)	150	65	67	BP
39	01:18:41	−73:25:47	−0.43	3.30 (2.8–3.9)	0 (< 1)	0.38	—	—	UN

No.	Names	Comments
1	N19, 0045−734, IKT2, W16, K61	SNR in HII region
2	IKT1, W18, K58	
3	AX J0049−729, K69	74.68 s
4	0047−735, IKT5, W22, K68	Contamination from No. 5
5	AX J0049−732, K70*	9.1321 s, contamination from No. 4
6		
7	K71	
8	AX J0051−733, K72	323.2 s, Be
9		
10		
11	AX J0051−722, K79†	91.1 s
12	0049−736, IKT6, W24, K77	
13	RX J0051.9-7311, IKT7, W25, K82	Be
14	RX J0052.1−7319, IKT8, W29, K84	Be, No detection of pulsations
15	1WGA J0053.8−7226, XTE J0053−724, IKT10, W34, K99	46.63 s, Be
16	XTE J0055−724, 1SAX J0054.9−7226, IKT11, W35, K103	59.00 s, Be
17	W36, K105	In the error circle of XTE J0054−720
18	IKT14, W39, K120	
19		
20	AX J0058−720, W41, K124*	280.4 s
21	0056−725, IKT16, W42, K128	
22	RX J0058.2−7231, K129	Be
23	K139	
24	N66, 0057−724, IKT18, W44, K140	SNR in HII region
25	RX J0059.2−7138	2.7632 s
26	IKT19, W45, K153	
27	K160	
28	W47, K166	
29	1SAX J0103.2−7209, AX J0103−722, 0101−724, IKT21, W50, K177	348.9 s (1997), a Be/X in the SNR
30	0102−723, IKT22, W51, K182	An O-rich young SNR
31	0103−726, IKT23, W52, K189	
32	AX J0105−722, DEM S128, IKT24, W53, K191	3.34300 s (significance=99.5%)
33		
34		Severe contamination from No. 30
35	K200	
36	W56, K202	
37	XTE J0111.2−7317	30.9497 s, Be
38	SMC X-1, W63, K242	0.70865 s (1993), B (Sk160)
		0.7100 s (1995)
		0.7065 s (1998)
39	W65	Galactic star HD8191

Chapter 6

Discussion

6.1 Classification with hardness ratio

6.1.1 XBPs and thermal SNRs in the SMC

So far we have classified the detected sources into two classes (XBPs and thermal SNRs), with the aid of their temporal/spectral properties and other information. In figure 6.1, we show the same plot as figure 5.2, but for only the sources of these classes. Sources of different classes are represented by different symbols. Here No. 14 (positionally coincident with the XBP RX J0052.1−7319) is excluded because we could not detect any sign of coherent pulsations from No. 14. We found that XBPs and thermal SNRs could be classified according to their HRs, although we have only four samples of thermal SNRs (0102−723 has been detected twice).

Using the X-ray flux instead of the raw count rate makes the figure more physical. On the other hand, HR can not be replaced with another quantity such as photon index or temperature, because several different models were used for the spectral fitting in section 5.3. Figure 6.2 shows the plot of HR against X-ray flux in 0.7–10.0 keV. For No. 29 (1SAX J0103.2−7209), the results obtained with the combined spectra are adopted. For No. 30 (0102−723), only the data obtained in 1993, in which the SNR is detected in the SIS field, were used.

6.1.2 Including the LMC samples

To get more samples, we included XBPs and thermal SNRs in the LMC from all the available data (40 observations as of 1998). Four known XBPs have been detected: LMC X-4, EXO 053109−6609.2, 1SAX J0544.1−710 and A0538−67. All of them have a long-term flux variability and a Be or O star as a companion (Bildsten et al. 1997; Burderi et al. 1998;

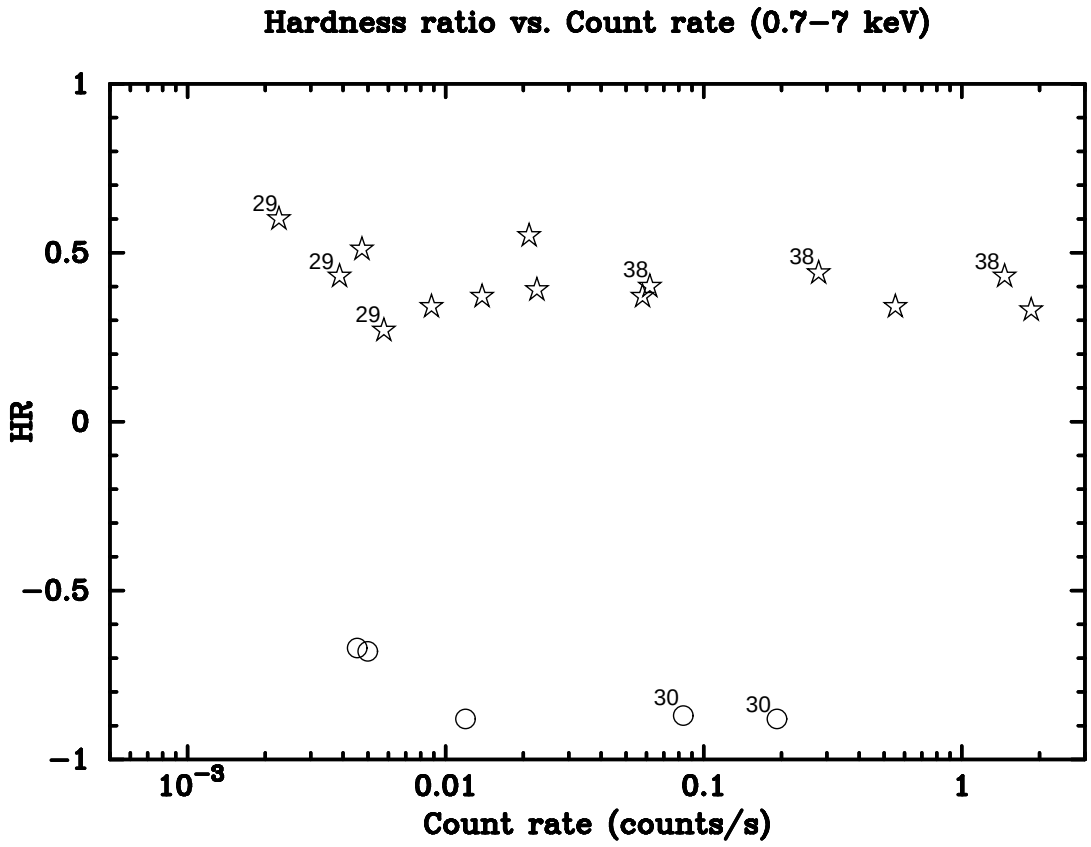

Figure 6.1: The plot of HR as a function of the detected (raw) count rate of GIS in 0.7–7.0 keV. Stars and circles represent XBPs and thermal SNRs in the SMC, respectively. The sources which were detected more than once are marked with the source number. Typical error of HR is ~ 0.1 at 0.005 counts/s, ~ 0.05 at 0.01 counts/s and $\lesssim 0.01$ at 0.1 counts/s.

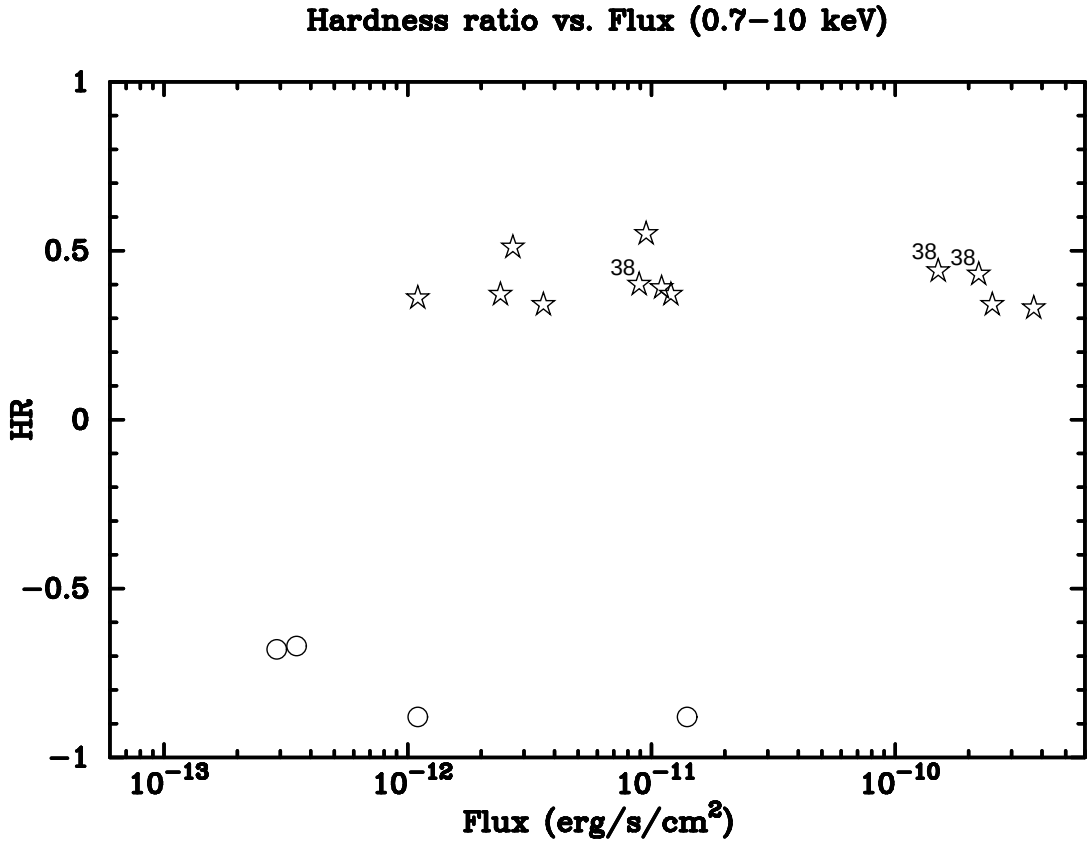

Figure 6.2: The plot of HR as a function of X-ray flux in 0.7–10.0 keV. Stars and circles represent XBPs and thermal SNRs in the SMC, respectively. SMC X-1 (detected three times) is marked with "38." Typical error of HR is ~ 0.1 at 5×10^{-13} erg s^{-1} cm^{-2}, ~ 0.05 at 1×10^{-12} erg s^{-1} cm^{-2} and $\lesssim 0.01$ at 1×10^{-11} erg s^{-1} cm^{-2}.

Cusumano et al. 1998 Haberl, Dennerl & Pietsch 1995). We could detect coherent pulsations only from the former three pulsars. Therefore we omitted A0538−67 from XBPs in this paper. Ten SNRs described in Hughes et al. (1995), Hayashi (1997) and Hughes, Hayashi & Koyama (1998), i.e. N103B, 0509−67.5, 0519−69.0, N23, N49, N63A, DEM71, N132D, 0453−68.5 and N49B, are undoubtedly thermal SNRs. In addition, ASCA has observed other SNRs: N44, N86, 0548−70.4, 0534−69.9 and 0543−68.9. We analyzed their spectra as described in subsection 5.3.2, then N44 and 0548−70.4 were classified as thermal SNRs. We also included other established classes, Crab-like SNRs (0540−69 and N157B) and blackhole candidates (LMC X-1 and LMC X-3).

We derived HRs of the three XBPs, 12 thermal SNRs, two Crab-like SNRs and two blackhole candidates in the LMC. To estimate the fluxes, we fitted the GIS spectra with simple models. An absorbed power-law model was adopted to XBPs, Crab-like SNRs and blackhole candidates, while an absorbed thin-thermal CIE plasma model was adopted to thermal SNRs. In the thermal plasma model, the global abundance was fixed to that of the interstellar matter in the LMC, i.e. 0.3 solar (Hayashi 1997; Hughes et al. 1998).

The line profiles of some thermal SNRs could not be reproduced by the simple thermal plasma model. However, the continuum shapes were well fitted, hence the derived fluxes have only a little error. To estimate the error, we fitted the GIS spectra of two thermal SNRs in the SMC, 0102−723 and 0103−726, with the same simple model. The global abundance was fixed to be that of the interstellar matter in the SMC, i.e. 0.2 solar (Russell & Dopita 1992). Since their diameters are 7.5 pc (0102−723) and 55 pc (0103−726) (Mathewson et al. 1983), they may be the representatives of young SNRs and old ones, respectively. The best-fit models well traced the continuum shapes, showing the same discrepancy in the line profiles. Derived fluxes in 0.7–10.0 keV were 1.3×10^{-11} erg s^{-1} cm^{-2} (0102−723) and 1.1×10^{-12} erg s^{-1} cm^{-2} (0103−726), respectively. On the other hand, the rather detailed analyses in subsection 5.3.2 yielded their fluxes as 1.4×10^{-11} erg s^{-1} cm^{-2} (0102−723) and 1.1×10^{-12} erg s^{-1} cm^{-2} (0103−726), respectively. Therefore the flux error due to the simplification of the model is estimated to be $\lesssim 10\%$. We do not need any higher accuracy in the flux estimation.

Figure 6.3 shows the plot of HR against the observed luminosity for the LMC and SMC samples. The definition of the observed luminosity $L_{\rm obs}$ is

$$L_{\rm obs} \equiv F_{\rm x} \times 4\pi d^2, \tag{6.1}$$

where $F_{\rm x}$ and d are the flux (0.7–10.0 keV) and the assumed distance (60 kpc for the SMC and 50 kpc for the LMC), respectively. The LMC samples (represented by filled symbols) largely

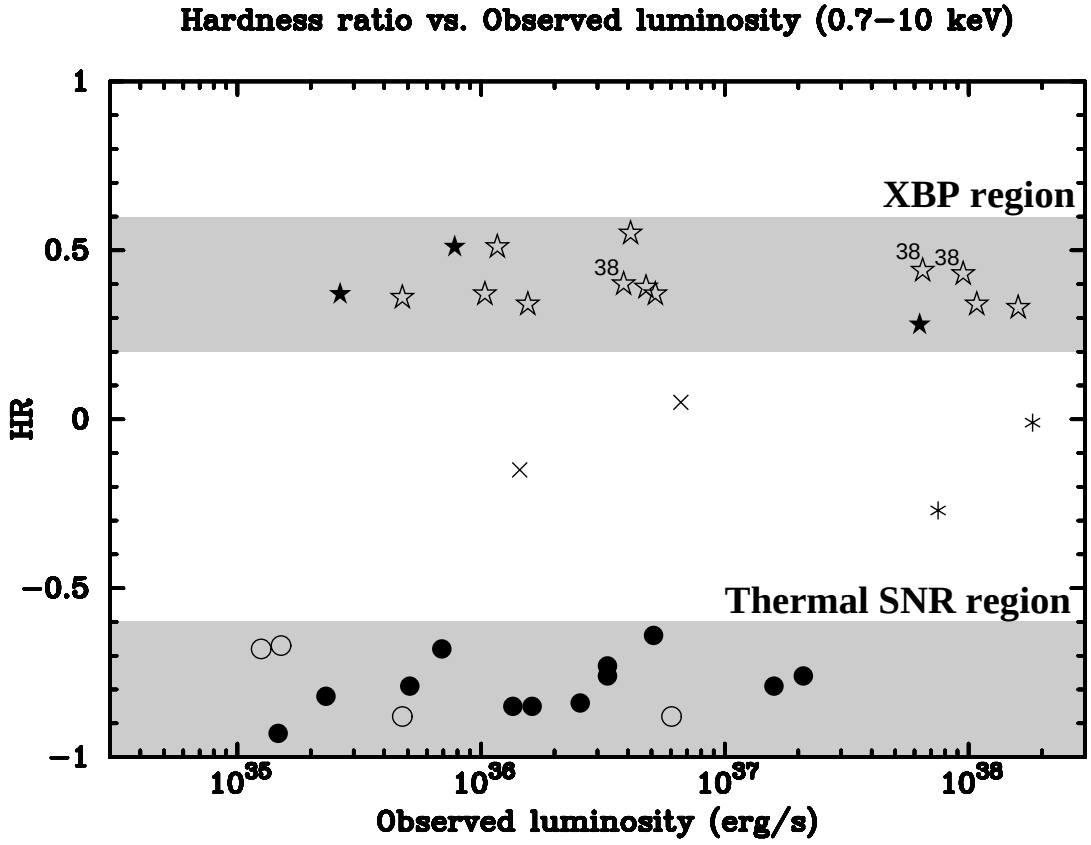

Figure 6.3: The plot of HR as a function of the observed luminosity in 0.7–10.0 keV. Open/filled symbols represent the SMC/LMC sources. Symbols represent XBPs (stars), thermal SNRs (circles), Crab-like SNRs (crosses) and blackhole candidates (asterisks), respectively. SMC X-1 (detected three times) is marked with "38." Typical error of HR is ~ 0.1 at 1×10^{35} erg s^{-1}, ~ 0.05 at 5×10^{35} erg s^{-1} and $\lesssim 0.01$ at 5×10^{36} erg s^{-1}.

enhanced the number of thermal SNRs, and now the split between XBPs and thermal SNRs is much clearer. Therefore we can safely say that HRs of all the XBPs in the SMC and LMC fall in a narrow region of $0.2 \leq \mathrm{HR} \leq 0.6$ ("XBP region"). On the other hand, those of all the thermal SNRs fall in a region of $-1.0 \leq \mathrm{HR} \leq -0.6$ ("thermal SNR region").

6.1.3 Validity of our classification method

Source classification with HR has been carried out with ROSAT data (K99). The common characteristic of the method of K99 and ours is that the HR is defined independently of any model: only the number of photons detected by ROSAT/ASCA detectors is used. Hence their/our HR is, so to speak, an "apparent hardness of the spectrum."

Such a simple method is not valid for X-ray sources in our Galaxy. The reason is that since soft X-rays are absorbed by the interstellar matter, HRs tend to be large for distant sources. To check this point, we simulated HRs of simple spectra of thin-thermal plasma or power-law under different absorption column densities. The temperature of the thin-thermal plasma model was set to be 0.5 keV (typical value for a thermal SNR), while the photon index of the power-law model was set to be 1.0 (typical value for an XBP). Absorption column density was set to be 3×10^{21} H cm^{-2} or 8×10^{22} H cm^{-2}, which correspond to a distance of 1 kpc (density 1 H cm^{-3} is assumed) or in the Galactic center region, respectively. The results are shown in table 6.1. It can be concluded that HR ranges widely for X-ray sources in our Galaxy, and that we can no longer distinguish between a nearby XBP and a distant thermal SNR.

On the other hand, the interstellar absorption is rather uniform towards the SMC and LMC (10^{20} –7×10^{21} H cm^{-2}, Luks 1994). HR of the thin-thermal plasma or the power-law ranges from -0.94 to -0.81 or from 0.25 to 0.48, respectively. Thus the classification with HR is valid for X-ray sources in the Magellanic Clouds.

Table 6.1: HRs of thin-thermal plasma (temperature = 0.5 keV) or power-law (photon index = 1.0) under different absorption column densities.

Model	$N_{\rm H}$ (H cm^{-2})	HR
Thermal plasma	3×10^{21}	-0.89
($kT = 0.5$ keV)	8×10^{22}	0.50
Power-law	3×10^{21}	0.36
($\Gamma = 1.0$)	8×10^{22}	0.96

The strong point of our method, when compared with that of K99, may be the simplicity. The classification criteria in K99 are more complicated: two kinds of hardness ratios and source extent are used. On the other hand, we need only one hardness ratio.

6.1.4 Candidates of XBPs and thermal SNRs

There is no exception in our classification method, i.e. no thermal SNR is in the XBP region and vice versa. In addition, other classes (Crab-like SNRs and blackhole candidates) do not intrude into the two regions. Hence we can define candidates of XBPs and thermal SNRs with high reliability: an unclassified source in the XBP (thermal SNR) region is a candidate of an XBP (thermal SNR).

Figure 6.4 shows the plot of HR against the observed luminosity for all sources in the SMC

and the classified sources in the LMC. No. 39 is omitted because it is identified with the Galactic star HD8191. In the figure, we can find eight XBP candidates and one thermal SNR candidate. Note that it is not meaningful to stick to the exact number of candidates, because their HR errors are not small (~ 0.2).

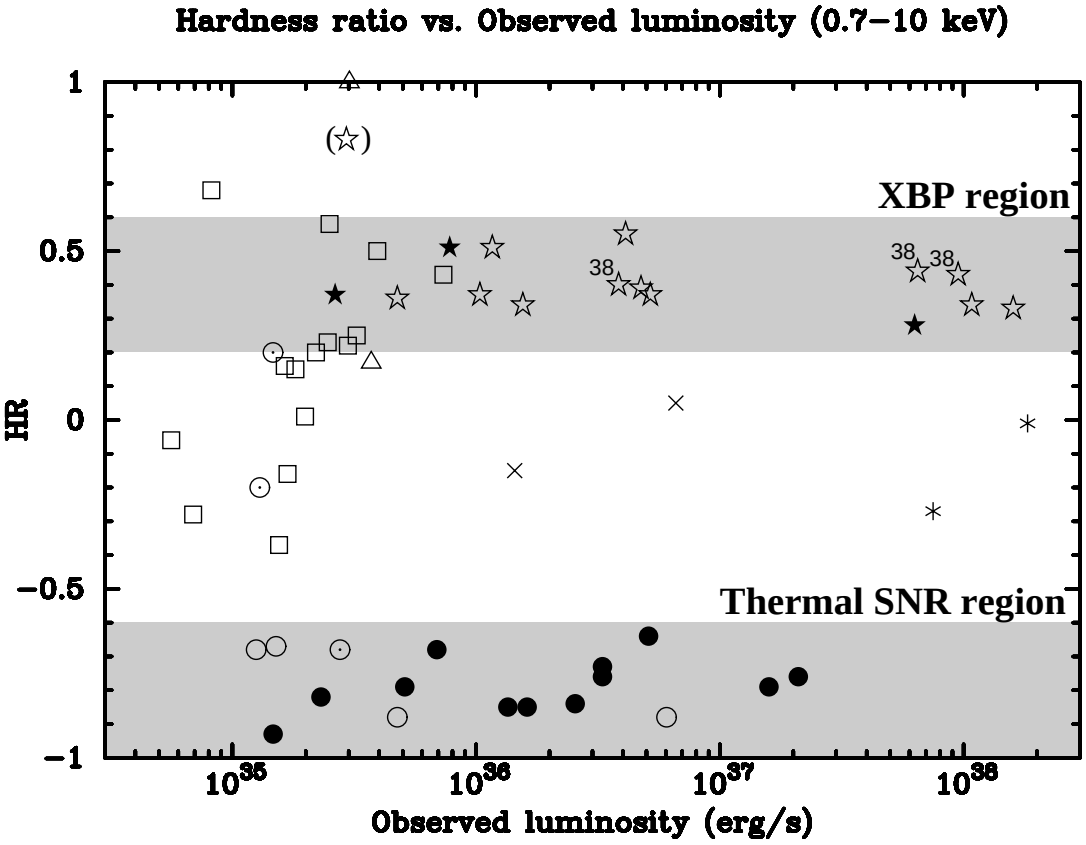

Figure 6.4: The plot of HR as a function of the observed luminosity in 0.7–10.0 keV. Open/filled symbols represent the SMC/LMC sources. Symbols represent XBPs (stars), thermal SNRs (circles), Crab-like SNRs (crosses), blackhole candidates (asterisks), other radio SNRs (dotted circles), non-pulsating HMXBs (triangles) and unknown sources (squares), respectively. SMC X-1 (detected three times) is marked with "38." The star in parentheses represents No. 14, which has been omitted from XBPs in this paper (see subsection 6.1.1). Typical error of HR of the latter three classes is ~ 0.2.

The eight XBP candidates have rather low fluxes. Therefore we could have not detect the pulsations due to the limited statistics even if they were really pulsating. The thermal SNR candidate is the radio SNR 0049−736. It was not classified as thermal in subsection 5.3.2 because of the limited photon statistics. We note that the other unclassified SNRs DEM S128

Table 6.2: Non-pulsating HMXBs in the SMC. Names and spectral types of the optical counterparts are shown.

Name	Optical	Ref.
RX J0032.9−7348	Blue	[1]
RX J0051.9−7311*	Be	[2][3]
SMC X-3	Be	[4]
RX J0052.9−7158	Be	[2][3]
SMC31 in WW92	Be	[2]
SMC X-2	Be	[1]
RX J0058.2−7231†	Be	[5]
1H0103−762	Be	[1][4]
RX J0106.2−7205	Be	[2][6]
EXO0114.6−7361	B	[2]
RX J0117.6−7330	Be	[8][9]

*: No. 13. †: No. 22.

References: [1]Kahabka & Pietsch 1996, [2]WW92, [3]Cowley et al. 1997, [4]van Paradijs 1995, [5]Schmidtke et al. 1998, [6]Hughes & Smith 1994, [7]Ye et al. 1995, [8]Clark, Remillard & Woo 1997, [9]Soria 1998.

(No. 32) and 0056−725 (No. 21) are out of the thermal SNR region. The fact confirms the possible non-thermal nature described in subsection 5.3.2. In addition, 0056−725 is an XBP candidate. Therefore X-rays from this source may be attributed to an (unresolved) XBP in the radio SNR 0056−725, as 1SAX J0103.2−7209 (No. 29).

6.2 Population in the SMC

As described in section 5.4 and the previous subsection, we have 13 XBPs and eight candidates in the SMC. Since most XBPs are HMXBs (e.g. Bildsten et al. 1997), in this section we assume all of the XBPs and the candidates to be HMXBs for the purpose of the population study. The number of non-pulsating HMXBs having an optical counterpart is at least 11 (summarized in table 6.2). Adding these numbers, we can count 32 HMXBs (including the eight candidates) in the SMC. On the other hand, there are about 70 HMXBs in our Galaxy (van Paradijs 1995; Bildsten et al. 1997; Nagase 1999).

No LMXB has been discovered in the SMC including this work, while our Galaxy is abundant in LMXBs: there are about 100 LMXBs (van Paradijs 1995).

Surveys of SNRs have been carried out in the radio band. So far 14 and 220 radio SNRs in the SMC and our Galaxy have been discovered (Mathewson et al. 1983; Mathewson et al. 1984; Mathewson et al. 1985; Filipovic et al. 1998; Green 1998). Among them, 0 and 7 are Crab-like

SNRs (e.g. Nagase 1999; Pavlov, Zavlin & Trümper 1999). The thermal SNR candidate defined in the previous subsection is the radio SNR 0049−736, hence the number of SNRs in the SMC remains unchanged. In our Galaxy, new SNR candidates have been discovered with ROSAT and ASCA. Over 100 SNRs may be discovered finally (e.g. Aschenbach 1996).

Table 6.3: Populations in the SMC and our Galaxy.

	HMXBs			LMXBs	SNRs		
	Non-pulse	XBPs	Candidates		Crab-like	Other	Candidates
SMC	11	13	8	0	0	14	0
SMC ×100*	1100	1300	800	0	0	1400	0
Galaxy	30	40	—	100	7	213	$\gtrsim 100$

*: Mass of the SMC is about 100 times less than that of our Galaxy.

The numbers of these classes in the SMC and our Galaxy are summarized in table 6.3. We also present the numbers in the SMC multiplied by 100, which is the mass ratio of the SMC to our Galaxy. Since our survey on the SMC is incomplete, the numbers of candidates give the lower limits. We could obtain sufficient photon statistics for the sources brighter than $\sim 1 \times 10^{-12}$ erg s^{-1} cm^{-2} (0.7–10.0 keV), which corresponds to $\sim 5 \times 10^{35}$ erg s^{-1}. Therefore our observations cover the luminosity ranges of typical HMXBs and LMXBs in our Galaxy. We make a comparison between these numbers.

First of all, the number of HMXBs normalized by the mass ratio is much higher in the SMC. It could not be due to a selection effect of the strong absorption in the Galactic Plane, because X-rays from HMXBs brighter than $\sim 5 \times 10^{35}$ erg s^{-1} can generally penetrate the matter of large column density. This fact indicates that there was an active starburst in the SMC several 10^{6-7} yr ago.

The number ratio of HMXBs to LMXBs exhibits a striking difference: 32/0 in the SMC (including the HMXB candidates) and 70/100 in our Galaxy. The difference has been already pointed out by Schmidtke et al. (1998), and is enhanced by our XBP candidates. Since a LMXB is considered to be formed when a neutron star is captured by a low-mass star, there is a time lag between the progenitorial supernova and birth of the LMXB. The time lag is estimated to be $\sim 3 \times 10^8$ yr even in high-density globular clusters and much longer in low-density globular clusters (Hut et al. 1992). On the other hand, a HMXB is formed soon after (less than $\sim 10^7$ yr) a supernova in a binary system of high-mass stars. Therefore, the very high ratio in the SMC may imply that it is not so long since the star-formation activity started in the SMC. In other words, LMXBs may be "not yet" formed in the SMC.

The number of Crab-like SNRs is suggestive. The number ratios of Crab-like SNRs to HMXBs in our Galaxy (7/70) and the SMC (0/32) are inconsistent with each other. Single or binary high-mass stars would have evolved into Crab-like SNRs or HMXBs, respectively. Therefore, if the inconsistency is real, it may imply that the efficiency of binary formation was much higher in the SMC than in our Galaxy. We should note that the number statistics are very poor and that the inconsistency may be due to a selection effect because the timing resolution was only 1 s for most sources in our analyses. Future observations with better photon statistics and a higher timing resolution will give the answer.

Chapter 7

Conclusion

We performed the systematic analyses on X-ray sources in the SMC with all the available data obtained with ASCA.

Among the 15 X-ray pulsars in the SMC, five were newly discovered during our analyses. We also confirmed the pulsations of other seven pulsars. We regarded 13 pulsars out of the 15 as XBPs because of their flux variability and, for some sources, the existence of the optical counterpart.

Eight radio SNRs were detected. The spectral analyses revealed that at least four SNRs were exhibiting the emission lines of ionized atoms, hence they were regarded as thermal SNRs. We note that other two SNRs are possibly emitting non-thermal X-rays.

We established a simple and reliable method of source classification with the hardness ratio (HR). XBPs fall in a range of $0.2 \leq \mathrm{HR} \leq 0.6$, while thermal SNRs fall in a range of $-1 \leq \mathrm{HR} \leq -0.6$. Including the LMC sources made the distinction much clearer.

With this method, eight XBP candidates and one thermal SNR candidate could be identified. We discussed the population in the SMC assuming that all the XBPs are HMXBs. The most striking difference is seen between the number ratio of HMXBs to LMXBs in the SMC and that in our Galaxy. The former is 32/0 and the latter is 70/100. We also pointed out that the number of Crab-like SNRs in the SMC (so far zero) may carry the key information on the efficiency of binary formation.

Acknowledgement

I am deeply grateful to Prof. K. Koyama for his continuous guidance throughout this study and the two years of my graduate course. I would like to sincerely thank my collaborators Mr. K. Imanishi, Mr. M. Tsujimoto and Ms. M. Nishiuchi, for their helpful discussion and sharing in data analyses. Analyses of the LMC data were carried out by them.

I also thank Dr. H. Tomida, Dr. K. Torii and Mr. M. Sakano for their instruction in the methods of data analyses. They were kind and patient enough to teach everything to a greenhorn like me. I express my thanks to Prof. F. Nagase, Dr. B. Paul and Dr. M. Ozaki, for the collaboration on the analysis of XTE J0111.2−7317. Prof. Nagase and Dr. Paul was also kind to proofread this thesis.

I thank all the members of the Cosmic-ray laboratory in Kyoto University for the daily discussion and insightful comments. People I met at many meetings and symposia also gave me helpful comments.

Finally, I would like to express my best gratitude to my friends and family, especially to my father. When I was depressed by certain terrible failure during this study, his calm and warm words encouraged me very much.

References

- Allen, W. H. et al. 1993, ApJ 403, 239
- Aschenbach, B. 1996, MPE report 263, 213
- Bildsten, L. et al. 1997, ApJS 113, 367
- Buckley, D. A. H., Coe, M. J., Stevens, J. B., Angelini, L., White, N. E. & Giommi, P. 1997, IAU Circ. 6789
- Burderi, L., Di Salvo, T., Robba, N. R., Del Sordo, S., Santangelo, A. & Segreto, A. 1998, ApJ 498, 831
- Burke, B. E., Mountain, R. W., Daniels, P. J., Dolat, V. S., & Cooper, M. J. 1994, IEEE Trans. Nucl. Sci., 41, 375
- Caldwell, J. A. R. & Coulson, I. M. 1986, MNRAS 218, 223
- Chakrabarty, D., Levine, A. M., Clark, G. W. & Takeshima, T. 1998a, IAU Circ. 7048
- Chakrabarty, D., Takeshima, T., Ozaki, M., Paul, B. & Yokogawa, J. 1998b, IAU Circ. 7062
- Clark, G., Doxsey, R., Li, F., Jernigan, J. G. & van Paradijs, J. 1978, ApJ 221, L37
- Clark, G. W., Remillard, R. A. & Woo, J. W. 1997, ApJ 474, L111
- Cook, K. 1998, IAU Circ. 6860
- Corbet, R., Marshall, F. E., Ozaki, M. & Ueda, Y. 1997, IAU Circ. 6803
- Cowley, A. P., Schmidtke, P. C., McGrath, T. K., Ponder, A. L., Fertig, M. R., Hutchings, J. B. & Crampton, D. 1997, PASP 109, 21
- Cusumano, G., Israel, G. L., Mannucci, F., Masetti, N., Mineo, T. & Nicastro, L. 1998, A&A 337, 772

- Filipovic, M. D. et al. 1998, A&AS 127, 119
- Gardiner, L. T., Sawa, T., & Fujimoto, M. 1994, MNRAS 266, 567
- Gardiner, L. T. & Noguchi, F. 1996, MNRAS 278, 191
- Girardi, L., Chiosi, C., Bertelli, G. & Bressan, A. 1995, A&A 298, 87
- Green, D. A. 1998, 'A Catalogue of Galactic Supernova Remnants (1998 September version)', Mullard Radio Astronomy Observatory, Cambridge, United Kingdom (available on the World-Wide-Web at "`http://www.mrao.cam.ac.uk/surveys/snrs/`")
- Haberl, F., Dennerl, K. & Pietsch, W. 1995, A&A302, L1
- Hayashi, I. et al. 1994, PASJ 46, L121
- Hayashi, I. 1997, Ph. D. thesis of Kyoto University
- Hughes, J. P. & Smith, R. C. 1994, AJ 107, 1363
- Hughes, J. P. 1994, ApJ 427, L25
- Hughes, J. P. et al. 1995, ApJ 444, L81
- Hughes, J. P., Hayashi, I. & Koyama, K. 1998, ApJ 505, 732
- Hurley, K. et al. 1999, ApJ 510, L111
- Hut, P. et al. 1992, PASP 104, 981
- Imanishi, K., Yokogawa, J. & Koyama, K. 1998, IAU Circ. 7040
- Irwin, M. J., Demers, S. & Kunkel, W. E. 1990, AJ 99, 191
- Israel, G. L. et al. 1997, ApJ 484, L141
- Israel, G. L. et al. 1998, IAU Circ. 6999
- Israel, G. L., Stella, L., Covino, S., Campana, S. & Mereghetti, S. 1999, IAU Circ. 7101
- Kahabka, P. Pietsch, W. & Hasinger, G. 1994, A&A 288, 538
- Kahabka, P. & Pietsch, W. 1996, A&A 312, 919
- Kahabka, P. & van den Heuvel, E. P. J. 1997, ARA&A 35, 69

- [K99] Kahabka, P., Pietsch, W., Filipovic, M. D. & Haberl, F. 1999, A&AS 136, 81
- Kahabka, P. 1999, IAU Circ. 7087
- Kahabka, P. & Li, X. -D. 1999, astro-ph/9902139
- Kouveliotou, C. et al. 1998, Nature 393, 235
- Kouveliotou, C. et al. 1999, ApJ 510, L115
- Koyama, K. et al. 1997, PASJ 49, L7
- Kroupa, P. & Bastian, U. 1997, New Astronomy 2, 77
- Lamb, R. C., Prince, T. A., Macomb, D. J. & Finger, M. H. 1999, IAU Circ. 7081
- Lochner, J. C., Marshall, F. E., Whitlock, L. A. & Brandt, N. 1998, IAU Circ. 6814
- Lochner, J. C. 1998, IAU Circ. 6858
- Lucke, R., Yentis, D., Friedman, H., Fritz, G. & Shulman, S. 1976, ApJ 206, L25
- Luks, T. 1994, Rev. Mod. Astr. 7, 171
- Marshall, F. E., Lochner, J. C. & Takeshima, T. 1997, IAU Circ. 6777
- Marshall, F. E. & Lochner, J. C. 1998, IAU Circ. 6818
- Masai, K. 1994, ApJ 437, 770
- Mateo, M. 1992, PASP 104, 824
- Mathewson, D. S., Cleary, M. N. & Murray, J. D. 1974, ApJ 190, 291
- Mathewson, D. S., Ford, V. L., Dopita, M. A., Tuohy, I. R., Long, K. S. & Helfand, D. J. 1983, ApJS 51, 345
- Mathewson, D. S., Ford, V. L., Dopita, M. A., Tuohy, I. R., Mills, B. Y. & Turtle, A. J. 1984, ApJS 55, 189
- Mathewson, D. S., Ford, V. L., Tuohy, I. R., Mills, B. Y., Turtle, A. J. & Helfand, D. J. 1985, ApJS 58, 197
- Mathewson, D. S. 1985, Proc. ASA 6, 104

- Mathewson, D. S., Ford, V. L. & Visvanathan, N. 1988, ApJ 333, 617
- McGee, R. X. & Newton, L. M. 1981, Proc. ASA 4, 189
- Murai, T. & Fujimoto, M. 1980, PASJ 32, 581
- Murakami, T., Kubo, S., Shibazaki, N., Takeshima, T., Yoshida, A. & Kawai, N. 1999, ApJ 510, L119
- Nagase, F. 1989, PASJ 41, 1
- Nagase, F. 1999, Proceedings of the international conference on the "Highlights in X-ray Astronomy" in honour of Joachim Trümper's 65th birthday (Garching, Germany, 17–19 June 1998), in press.
- Ohashi, T., et al. 1996, PASJ 48, 157
- Pavlov, G. G., Zavlin, V. E. & Trümper, J. 1999, ApJ 511, L45
- Price, R. E., Groves, D. J., Rodrigues, R. M., Seward, F. D., Swift, C. D. & Toor, A. 1971, ApJ 168, L7
- Putman, M. E. et al. 1998, Nature 394, 752
- Raymond, J. C. & Smith, B. W. 1977, ApJS 35, 419
- Russell, S. C. & Dopita, M. A. 1992, ApJ 384, 508
- Santangelo, A. et al. 1998, IAU Circ. 6818
- Sawa, T., Fujimoto, M. & Kumai, Y. 1999, Proceedings of the IAU Symposium #190, "New Views of the Magellanic Clouds" (Victoria, British Columbia, Canada, 12–17 July 1998), in press.
- Schmidtke, P. C. et al. 1999, AJ 117, 927
- Schmidtke, P. C. & Cowley, A. P. 1998, IAU Circ. 6880
- Serlemitsos, P. J., et al. 1995, PASJ 47, 105
- Soria, R. 1998, astro-ph/9810028
- Sreekumar, P. & Fichtel, C. E. 1991, A&A 251, 447

- Sreekumar, P. et al. 1992, ApJ 400, L67
- Sreekumar, P. et al. 1993, Phys. Rev. Lett. 70, 127
- Tanaka, Y., Inoue, H. & Holt, S. S. 1994, PASJ 46, L37
- van Paradijs, J., 1995, in "X-Ray Binaries", ed. W. H. G. Lewin, J. van Paradijs & E. P. J. van den Heuvel (Cambridge University Press: Cambridge), 536
- Vallenari, A., Chiosi, C., Bertelli, G. & Ortolani, S. 1996, A&A 309, 358
- [WW92] Wang, Q. & Wu, X. 1992, ApJS 78, 391
- Wilson, C. A. & Finger, M. H. 1998, IAU Circ. 7048
- Wojdowski, P., Clark, G. W., Levine, A. M., Woo, J. W. & Zhang, S. N. 1998, ApJ 502, 253
- Ye, T., Amy, S. W., Wang, Q. D., Ball, L. & Dickel, J. 1995, MNRAS 275, 1218
- Yokogawa, J. & Koyama, K. 1998a, IAU Circ. 6835
- Yokogawa, J. & Koyama, K. 1998b, IAU Circ. 6853
- Yokogawa, J. & Koyama, K. 1998c, IAU Circ. 7028
- Yokogawa, J. & Koyama, K. 1998d, IAU Circ. 7009